Macromolecules

Article

pubs.acs.org/Macromolecules

Dynamics of Branched Polymers: A Combined Study by Molecular Dynamics Simulations and Tube Theory

Petra Bačová,[†] Laurence G. D. Hawke,[‡] Daniel J. Read,[‡] and Angel J. Moreno*[,⊥,§]

[†]Departamento de Física de Materiales, Universidad del País Vasco (UPV/EHU), Apartado 1072, 20080 San Sebastián, Spain

[‡]Department of Applied Mathematics, University of Leeds, LS2 9JT Leeds, U.K.

[⊥]Centro de Física de Materiales (CSIC, UPV/EHU) and Materials Physics Center MPC, Paseo Manuel de Lardizabal 5, 20018 San Sebastián, Spain

[§]Donostia International Physics Center, Paseo Manuel de Lardizabal 4, 20018 San Sebastián, Spain

ABSTRACT: We present large-scale computer simulations of entangled polymers with symmetric star-like and Cayley tree-like architectures. Unlike the usual observation for reptational behavior of linear chains, the simulated systems exhibit a strong dispersion, over several decades, of the relaxation times after the local reptative ("Rouse in tube") regime. Relaxation is dramatically slowed down by approaching the branch point from the outer segments. This is consistent with the expected retraction mechanism for strongly entangled branched polymers. In order to describe fluctuations around the branch point, we introduce a Rouse-like model adapted to star-like polymers and incorporate entanglements by means of localizing springs. Model predictions for localization of the branch point are compared with simulations with fixed arm ends, which suppress retraction and tube dilution. Strikingly, the simulations reveal a localization of the branch point weaker than expected. This may be due to an early tube dilation process, or exploration of the branch point along the tubes of the confining arms. We quantify, as a function of time, the strength of such effects and the fraction of relaxed material directly from the simulations with free ends. This allows us to renormalize the tube diameter and entanglement time in our model as time-dependent quantities. With this renormalization, the model provides an excellent description of the early relaxation of the branch point.

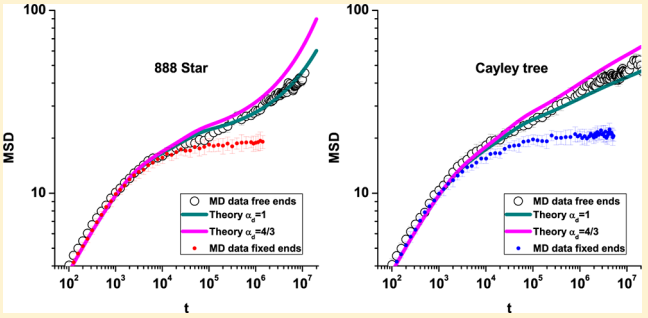

1. INTRODUCTION

In the melt state, a polymer chain is mutually entangled with other chains experiencing topological constraints. The tube model[1] represents these entanglements as an effective tube, where the chain is confined. The confinement length, i.e., the so-called tube diameter a, is a parameter of the model and represents the end-to-end distance of a chain of molecular weight identical to the entanglement mass M_e. The tube theory disregards the finer details of the structure of the confined chain at length scales smaller than a, and replaces the chain by a random walk, called the primitive path, of step length a. The primitive path is interpreted as the shortest path between the chain ends that is compatible with the topological constraints. According to the original tube model,[1] the only available relaxation mechanism for the primitive path is diffusion back and forth along the tube axis. This mechanism is commonly known as reptation. To resolve substantial discrepancies between the original model and experiments, refined tube models for linear chains[2−5] incorporate additional relaxation mechanisms of the primitive path, such as contour length fluctuations (CLF) and constraint release (CR). The mechanism of CLF accounts for the rapid and shallow fluctuations occurring at the free ends of the primitive path before reptative modes set in.[2,6] CR models the hops that the primitive path undergoes when tube constraints are removed due to motion of the surrounding chains.[2−5]

The tube model has been extended to model branched topologies like star polymers,[7,8] H-polymers,[9,10] pom-pom molecules,[11] combs,[12−16] Cayley trees,[17,18] DendriMacs,[19] and topologies of industrial complexity.[20,21] These complicated architectures contain one or more branch points, that are responsible for their complex viscoelastic and dynamic properties as compared to linear chains. Reptation in branched systems remains inactive until the late stage of relaxation, or may be fully suppressed in symmetric architectures with a central branch point (e.g., Cayley trees). According to theory,[2] relaxation before the onset of reptation occurs via arm retraction. The mechanism of arm retraction is analogous to CLF in linear polymers, though involves deeper fluctuations and is exponentially rare as relaxation approaches a branch point from the outer segments. Topologies of industrial complexity which contain many layers of branch points relax

Received: March 21, 2013
Revised: May 2, 2013
Published: May 29, 2013

   dx.doi.org/10.1021/ma4005988 | *Macromolecules* 2013, 46, 4633−4650

hierarchically.[2,20] Hierarchical relaxation means that once free ends retract back to the outermost layer of branch points, these become mobile, activating deeper retractions toward the second layer, and so on. If the macromolecular architecture is asymmetric (e.g., T-shaped stars), the late relaxation occurs via reptation of an effective linear chain, in which all relaxed branches act as frictional beads. Regarding CR in branched polymers, the evidence for an extremely broad, exponential distribution of relaxation times gave rise to the tube dynamic dilution (DD) hypothesis.[2] In the DD picture, the CR events arising during the retraction of the branches lead to a slow, progressive dilution of the effective entanglement network. This is modeled as a time-dependent widening ("dilation") of the tube. The dilated tube diameter at each time step is determined by the respective fraction of relaxed material.

Recently, Read et al.[22] proposed that the tube could be visualized as the "mean-path" (which is the path connecting the average position of monomers). Chain segments fluctuate about this mean path. Using the Warner−Edwards model,[23,24] they showed that this gives a smooth curve in space. The smoothness of the mean path is set by a free energy and is directly related to the fact that bending is penalised. Moreover, the considered free energy maintains Gaussian statistics at all length scales.

MD simulations examine directly the multichain problem and provide a powerful methodology to study the dynamics of polymer chains in the melt state. A readily obtained observable from the MD simulations is the mean square displacement (MSD), which provides significant information about the dynamics of the polymer chain. Previous MD simulations on linear chains[25−28] show that the MSD of central monomers obeys the predictions of the tube model whereas end monomers obey faster dynamics.[25,27,28] MD studies on branched polymer melts have been scarce due to their high computational cost. There are two main reasons for this: the much longer characteristic times of branched polymers as compared to linear chains and, subsequently, the difficulty to equilibrate the macromolecular configurations. Fortunately, efficient methods combining Monte Carlo (MC) and MD simulations have been developed recently to equilibrate large-scale conformations with low computational cost.[29] These equilibration methods, together with high parallelization, make MD simulations on entangled branched architectures plausible with modern computational resources. The simulation work of Zhou and Larson[30] focused on the branch point motion in melts of asymmetric star polymers and brought to light a new concept of branch point relaxation. It was shown that, while at the short time scales branch point remains confined within the tube diameter, at time scales longer than the relaxation time of the short arm the branch point can explore the space by taking random hops along the tube.

Here we present large scale MD simulations of entangled polymers of linear, symmetric star-like and Cayley tree-like topology. The obtained MSD reveals a dramatic influence of the topology on the dynamics of the chain, and provides strong evidence of arm retraction. We focus on the dynamics of the branch point of the star polymer and of the central branch point of the Cayley tree, both in the presence and absence of standard constraint release. The latter is achieved by performing MD with free and fixed chain ends, respectively. To provide a basic model with which to compare MD results, we have derived analytical expressions describing local motion of branched chains subject to entanglement constraints. The model is based on the Warner−Edwards[23,24] picture of the tube, in which entanglements are represented by localizing springs. We find that localization of the branch point in the simulations with fixed ends is weaker compared to our model predictions, suggesting some relaxation of the entanglement constraints experienced by the branch point (e.g., an early tube dilation process occurs). We quantify the standard CR by computing directly the tube survival probability from the MD. It is shown that our model, after the inclusion of CR events and early tube dilation, provides an excellent description of the MSD of the branch points within the simulation time window. This finding strongly supports the physics underlying the "dynamic dilution" hypothesis. The remainder of the article is structured as follows. Section 2 gives details of the MD simulation method while section 3 presents general observations from the MD results. Section 4 outlines the theory and summarizes the obtained expressions for the MSD (the full calculation for the unentangled and entangled case is detailed in Appendix A and B, respectively). Section 5 discusses the dynamics of the branch points both in the presence and absence of CR events. Conclusions are given in section 6.

2. SIMULATION DETAILS

The simulated systems were modeled according to the well-known scheme proposed by Grest and Kremer.[25] In this coarse-grained model, the chains are represented as strings of beads ("monomers") connected by springs, with generic interactions describing excluded volume and connectivity (see below). Figure 1 shows a schematic representation of the architectures

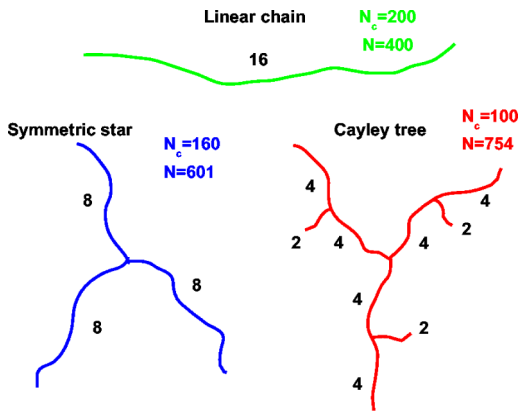

Figure 1. Illustration of the simulated systems: N_c denotes the number of the polymers in the simulation box. N is the number of beads per macromolecule. The numbers labeling backbones and branches denote the respective lengths, expressed as multiples of the entanglement segment $N_e = 25$.

of the simulated systems. These are linear chains, 3-arm symmetric stars and Cayley trees. The numbers associated with each backbone and branch in Figure 1 represent the respective number, Z, of entanglement segments. The corresponding number of monomers is ZN_e, with N_e the entanglement length, i.e., the number of monomers per entanglement segment. For the specific model simulated in this work, we have $N_e = 25$, though it should be noted that there is some uncertainty in the value depending on how it is estimated (see below).

As can be seen in Figure 1 the maximum distance between two outermost monomers of different branches in the stars and Cayley trees is, in all cases, $Z = 16$ entanglement segments. This

dx.doi.org/10.1021/ma4005988 | Macromolecules 2013, 46, 4633−4650

is identical to the length of the linear chains. Simulation of these three selected systems can provide useful information about the effect of branching on the chain dynamics. Indeed, the 3-arm star is obtained by attaching a branch of length $Z = 8$ to the center of the linear chain. Likewise, the Cayley tree is obtained by attaching branches of length $Z = 2$ to the centers of the star arms.

As aforementioned, in the Grest-Kremer model the monomeric units are represented by beads. The excluded volume interaction is given by a purely repulsive Lennard-Jones (LJ) potential:

$$U_{LJ}(r) = \begin{cases} 4\varepsilon\left[\left(\frac{\sigma}{r}\right)^{12} - \left(\frac{\sigma}{r}\right)^{6} + \frac{1}{4}\right], & \text{for } r \le r_c, \\ 0, & \text{for } r > r_c, \end{cases} \quad (1)$$

with a cutoff distance $r_c = 2^{1/6}\sigma$. The LJ diameter σ is the length unit of the model. The temperature unit is ε/k_B, with k_B the Boltzmann constant. The time unit is given by $\tau_0 = (m_0\sigma^2/\varepsilon)^{1/2}$, with m_0 the monomer mass. Connectivity between consecutive beads is provided by a finite-extension nonlinear elastic (FENE) potential:

$$U_F = -\frac{1}{2}K_F R_F^{\,2} \ln\left[1 - \left(\frac{r}{R_F}\right)^2\right] \quad (2)$$

We use $K_F = 30\varepsilon/\sigma^2$ for the spring constant and $R_F = 1.5\sigma$ for the maximum bond length. Furthermore, a certain degree of chain stiffness is introduced by applying a bending potential

$$U_{bend}(\theta) = k_\theta(1 - \cos\theta) \quad (3)$$

where θ is the bending angle between three consecutive monomers ($\theta = 0$ for a rod). We have used a bending constant $k_\theta = 2\varepsilon$. With this choice, long linear chains have a characteristic ratio $C_\infty = \lim_{N\to\infty}\langle R_e^{\,2}\rangle/Nl_0^{\,2} = 3.6$ at the investigated temperature and density (see below). In the former expression R_e and N are the end-to-end distance and the number of monomers per chain, respectively, while $l_0 = 0.97\sigma$ is the average bond length. The value $C_\infty = 3.6$ is higher than in flexible bead−spring chains ($k_\theta = 0$, $C_\infty = 1.76$) and lower than in common polymers as polyisoprene or polybutadiene ($C_\infty \sim 5$).

The introduction of some local stiffness has the advantage of decreasing the entanglement length N_e. This reduces computational cost since we can simulate, with the same chain length N, more strongly entangled systems than by using flexible chains. For the semiflexible chains investigated in this work ($k_\theta = 2\varepsilon$) one finds $N_e \approx 25$. A primitive path analysis gives $N_e^{PP} = 23$,[31] whereas an estimation from the monomer mean square displacement (MSD) gives $N_e^{MSD} = 27$.[30] These are considerably smaller than the values found for flexible chains[28] ($k_\theta = 0$; $N_e^{PP} = 65$, $N_e^{MSD} = 50$).

On the other hand, we aim to compare simulation results with tube-based models that are formulated for Gaussian chains. Therefore, the chain stiffness introduced by the bending potential should not be too strong, since local deviations from Gaussianity should not persist at contour distances beyond the entanglement length. The simulated case constitutes a good compromise between a relatively short entanglement length and a short-range of non-Gaussian effects. Indeed we have checked that, if $R(|n - m|)$ is the distance between the nth and mth monomer, the limit $\langle R^2(|n - m|)\rangle/|n - m|l_0^{\,2} \approx C_\infty$ is already found for $|n - m| \sim N_e$.

All the simulations were performed at temperature $T = \varepsilon/k_B$ and number density $\rho = (NN_c)/V = 0.85\sigma^{-3}$, with N_c the number of macromolecules in the simulation box of volume V, and N the number of monomers per macromolecule. The former density corresponds to melt conditions in bead−spring polymers. We used boxes with a total of 80000, 96160, and 75400 monomers for the systems of linear chains, stars and Cayley trees, respectively. Before the production run, the system has to be equilibrated properly. The time scales for equilibration of the long and branched macromolecules simulated here are far beyond the current computational capabilities by using standard MD. However, efficient methods combining Monte Carlo (MC) and MD simulations have been developed to equilibrate large-scale conformations with low computational cost. We used a very similar method to that proposed by Auhl et al.[29] Thus, we first equilibrated, by standard MD, systems of small linear chains and 3-arm symmetric stars, with a length of one entanglement per linear backbone or star arm. These were used as building blocks to construct the long branched macromolecules with the desired architecture. The bending angles at the junction points of different building blocks were selected so that the macromolecular conformation obeyed the correct target function[29] $C([n - m|) = \langle R^2(|n - m|)\rangle/|n - m|l_0^{\,2}$ (see ref 29 for details).

Afterward, we placed randomly the generated macromolecules in the simulation box, and followed the prepacking procedure proposed by Auhl et al.[29] This consists of an MC simulation in which the macromolecules are treated as rigid objects performing large-scale motions (rotations, translations, reflections, etc.) that are accepted only when they reduce the local density fluctuations.[29] After a significant reduction of the inhomogeneities, we performed a short MD run ($\sim 10^6$ steps, with a time step $\Delta t = 0.001\tau_0$) in which force-capping[29] was applied to the LJ interaction of eq 1. The capping radius was slowly reduced and finally the full LJ interaction was switched on. The equilibration was finished with a standard MD run of about 10^8 time steps. We checked that the obtained configurations obeyed the target function $C([n - m|)$. The time step for this last equilibration run as well as for the production runs was $\Delta t = 0.01\tau_0$.

The MC simulations were performed by using a homemade code. The MD simulations were performed by using the ESPResSo simulation package.[32] All the runs were performed at constant volume. In the MD runs, the temperature was controlled by the Langevin thermostat with a friction constant $\Gamma = 0.5m_0/\tau_0$ and the equations of motion were integrated by using the velocity−Verlet algorithm. The equilibration runs were performed serially (for MC) or with low paralellization (for MD). The production MD runs extended over unusually long time scales (up to 3×10^9 time steps) and required high parallelization. The estimated total CPU time for the production runs was of 10^6 h.

3. INITIAL OBSERVATIONS FROM SIMULATION RESULTS

The time evolution of the monomer mean square displacement (MSD), $\langle \Delta r^2(t)\rangle$, provides valuable information about the microscopic dynamics of the system. This quantity, which is often difficult to access in experiments, can be easily computed from the simulation data. Moreover, by computing the MSD of specific segments along the macromolecule, we may shed light

dx.doi.org/10.1021/ma4005988 | Macromolecules 2013, 46, 4633−4650

on the role of the macromolecular architecture on the internal relaxation mechanisms. In our analysis of the simulation data, we have divided the macromolecules into segments of length equal to one entanglement (N_e = 25 monomers). The corresponding MSD of different segments in the three investigated systems are shown in Figures 2 and 3. We note

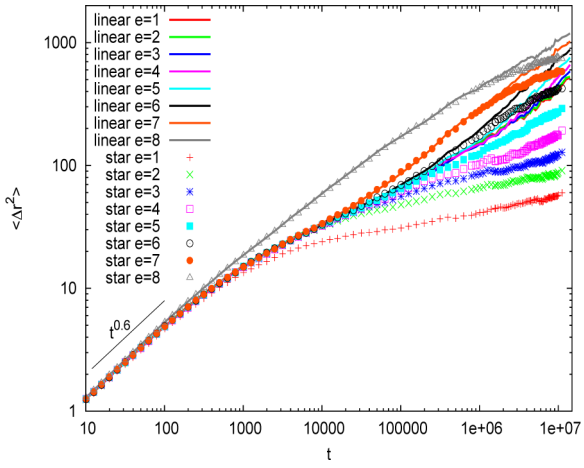

Figure 2. MSD of the entanglement segments (see text) in the linear chains and symmetric stars.

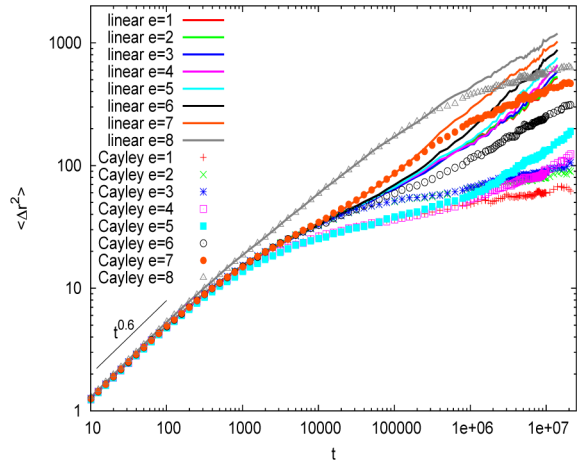

Figure 3. MSD of the entanglement segments (see text) in the linear chains and Cayley trees.

that in Figures 2 and 3, as in all figures in the remainder of the article that contain MD data, the time axis is expressed in simulation units τ_0. The notations in the legends for the different data sets must be understood as follows. We treat the linear chain as a 2-arm star with the branch point in the center of the backbone, i.e., the arms have Z = 8 entanglement segments, as in the 3-arm stars. We label the entanglement segments in each arm of the linear chains and stars as e = 1, 2, ..., 8, by following the path from the branch point to the outermost monomer in the same arm. Obviously, for each entanglement segment in a given arm there are, by symmetry, other equivalent segments in the other arms and accordingly the corresponding MSD is averaged over them. In the case of the Cayley trees we do not include in Figure 3 the data for the short side branches (Z = 2), and the entanglement segments are labeled in the same way as in the linear chains and stars. Thus, we label the segments as e = 1, 2, ..., 8, by following the path of length Z = 4 from the central branch point to one of the three outer ones, and from there to the outermost monomer in the same branch of Z = 4 (see Figure 1). Again, the MSD is averaged over equivalent segments in the three long arms.

In Figure 2 we compare data of the linear chains and symmetric stars. In Figure 3, the comparison is done for the linear chains and Cayley trees. Up to the entanglement time $\tau_e \approx 1800$ (see ref 30), the MSD of the different segments follow Rouse behavior. The data are better described by an effective power-law $\langle \Delta r^2 \rangle \sim t^{0.6}$ than by the strictly Rouse-like behavior $\langle \Delta r^2 \rangle \sim t^{1/2}$. This small difference may originate from non-Gaussian correlations (not included in the Rouse model) at $N < N_e$, which are related to the semiflexible character introduced by the bending potential (see above).

At the entanglement time $\tau_e \approx 1800$ the different segments start to probe the topological constraints, and the MSD progressively deviates from the Rouse behavior. In the usual picture for linear chains, the initial fluctuations of the monomer along the primitive path are described as Rouse dynamics of the curvilinear coordinate ("Rouse in tube" dynamics). The consequence of this for the real-space monomer dynamics is that the MSD scales as $\langle \Delta r^2(t) \rangle \sim t^{1/4}$. As aforementioned, the Rouse regime $\langle \Delta r^2(t) \rangle \sim t^x$ in our system is characterized by an exponent x = 0.6 instead of the ideal value x = 1/2. Accordingly, we may expect that the characteristic exponent for the "Rouse in tube" dynamics is x = 0.3 instead of the ideal value x = 1/4. Figures 4 and 5 show the ratio $\langle \Delta r^2(t) \rangle / t^{0.3}$. In

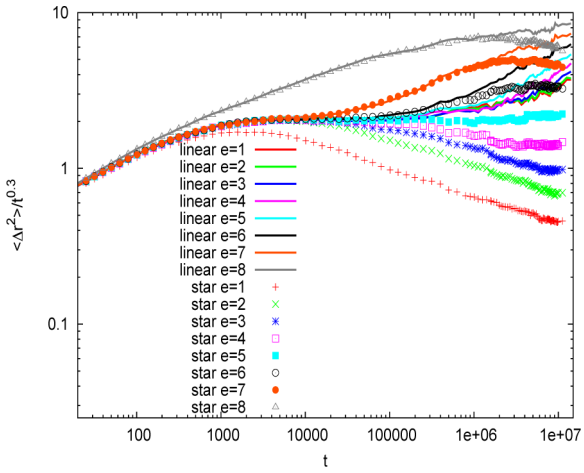

Figure 4. MSD of the entanglement segments in the linear chains and symmetric stars normalized by $t^{0.3}$.

this representation the "Rouse in tube" regime is recognized as a plateau for $t > \tau_e$. Most of the segments in the three investigated architectures exhibit this behavior for at least a portion of the time window $\tau_e < t < \tau_R$, where τ_R is the Rouse time, i.e., the time scale for the longest internal chain modes.[1] This can be estimated as $\tau_R = \tau_e(N_a/N_e)^2 \approx 10^5$, with N_a = 200 the number of monomers per long arm. Data of some specific segments do not obey the mentioned overlap, namely the outermost segments (e = 8) and the segments directly attached to the branch points (e = 1 in stars and Cayley trees, as well as e = 4 and 5 in Cayley trees).

In the case of the outermost segments e = 8, the data reveal a much faster behavior than the plateau regime $\langle \Delta r^2(t) \rangle / t^{0.3} \sim t^0$. This can be understood as follows. The intramolecular conformation can perform strong fluctuations in the neighbor-

dx.doi.org/10.1021/ma4005988 | Macromolecules 2013, 46, 4633−4650

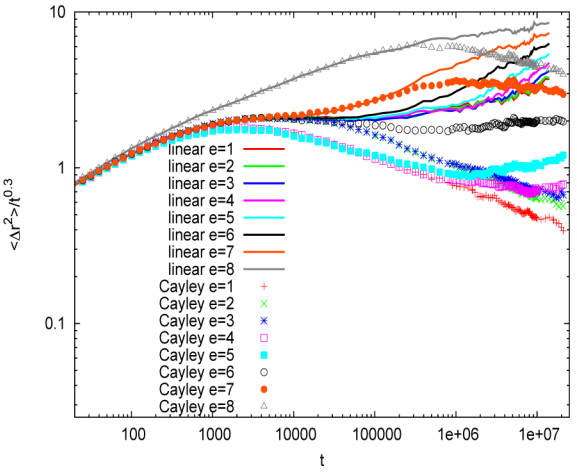

Figure 5. MSD of the entanglement segments in the linear chains and Cayley trees normalized by $t^{0.3}$.

hood of the free ends, since the segments there are weakly affected by the topological constraints. As a consequence, the primitive path near the chain ends is almost fully relaxed by simple Rouse dynamics at $t < \tau_e$. As can be seen in Figures 2 and 3 the initial Rouse behavior is indeed weakly perturbed up to time scales of $t \sim \tau_R \gg \tau_e$. Moreover this feature does not depend on the specific intramolecular architecture up to long time scales. Thus, the MSD of the outermost segments e = 7,8 of the linear chains is indistinguishable from the corresponding data for the stars and Cayley trees up to times of $t \geq \tau_R$. In summary, for times $t < \tau_R$, the outermost segments do not probe the specific relaxation mechanisms associated with each intramolecular architecture. For longer times, the MSD of the outer segments of both the star and Cayley tree architectures is smaller than that of the corresponding segments of the linear chain. This is because the outer segments remain attached to more slowly relaxing inner sections of chain; although they can easily escape their own tube constraints, they cannot move large distances because of entanglement constraints on the rest of the chain.

In the case of the segments directly attached to the branch points, the data exhibit a clear slowing down with respect to the 'Rouse in tube' dynamics of other segments. We will see that this effect essentially originates from the 3-fold connectivity of the branch point, and that branch point dynamics can still be explained by considering local Rouse motion in a tube (see section 4.2).

Thus, with the mentioned exception of the outermost segments, the MSD exhibits universal "Rouse in tube" dynamics over a certain time window after the entanglement time, even if the segments are not placed in linear chains but in arms of branched architectures. However, rather evident differences between the different architectures emerge at longer times $t > \tau_R$. Thus, the overlap in the MSD of the inner segments ($e < 3$) persists in the linear chains, and the scaling behavior changes from $\langle \Delta r^2(t) \rangle \sim t^{0.3}$ to $\langle \Delta r^2(t) \rangle \sim t^{1/2}$. These features are consistent with the expected reptational mechanism for inner segments at long times. In contrast with the observation for linear chains, the MSD for $t > \tau_R$ spreads out dramatically in the stars. Since the three long arms ($Z = 8$) are equivalent and relax in the same time scale, there is not a common tube over which the whole star can reptate at long times. Instead, relaxation occurs by deep contour length fluctuations (arm retraction). Because this mechanism involves a large entropic cost, the mobility of the segments in the stars is progressively reduced as the branch point is approached. The data in Figure 2 evidence a broad distribution of relaxation times along the arm contour. Thus, at the end of the simulation ($t \sim 2 \times 10^7$) the difference between the MSD of the outermost and innermost segments of the star arms is about a factor 10. The expected ultimate merging of all data sets will occur at time scales far beyond the simulation limits.

For the same reason discussed above, reptation in Cayley tree is not possible either. Again, relaxation occurs via arm retraction, leading to variation in mobility along the arm contour. However, unlike in stars, this variation is not monotonic with respect to the location of the segment along the arm. Thus, in a broad dynamic window the segments directly attached to the outer branch points (e = 4,5) are more restricted than some inner segments that are closer to the central branch point (e = 2,3) (see Figures 3 and 5). This behavior is found at time scales before full relaxation of the short side branches. This can be estimated from the normalized orientational correlator (not shown) $P(t) = \langle \mathbf{e}_s(t) \cdot \mathbf{e}_s(0) \rangle / \langle e_s^2(0) \rangle$, where $\mathbf{e}_s$ is the end-to-end vector of the short side branch. We find $P(t) < 0.05$ for $t > 10^6$. At much longer times after full relaxation of the short branches, the MSD of the different segments of Cayley tree recovers the monotonic behavior of the segment mobility with respect to location of the segment along the arm, as observed in the stars, i.e., segments e = 4,5 now have a larger MSD than segments e = 2, 3. This feature can be clearly seen in the $\langle \Delta r^2(t) \rangle / t^{0.3}$ representation in Figure 5 and is consistent with the idea of hierarchical relaxation. After the short side branches relax, they act as source of extra friction, for motion of the main arms, and the Cayley tree is reduced to an effective symmetric star.

4. THEORY

4.1. Rouse Dynamics. To provide a basic model with which to compare simulation results, we have derived expressions for the MSD of monomers in the Rouse model for star polymer architectures. These expressions have been obtained for both free chains and, in order to model localization due to entanglements, chains where monomers are localized by a quadratic potential[22−24,33−35] (see next subsection). A similar calculation was attempted for linear chains by Vilgis and Boué,[33] but their expressions do not reduce to the Gaussian chain result at equilibrium because they do not include the contribution of the mean path. Our equations derived below correct this point, and can be used for linear chains if these are treated as two-arm stars. By using the continuous chain Rouse model, we are explicitly ignoring some complications inherent to the molecular dynamics model, such as the discrete nature of the beads or the bending potential (eq 3). Nevertheless, the expressions derived here provide a starting point for the analysis of monomer motion near branch points in the MD simulations. It must be stressed that these expressions refer only to local branch point motion within the tube and not to the diffusive steps[2,30,36,37] (curvilinear hopping) that a branch point undertakes after an arm has fully escaped from its tube.

For an unentangled star polymer, the Langevin equation and the free energy read, respectively[1,38]

$$\zeta_0 \frac{\partial \mathbf{r}_{\alpha,l,t}}{\partial t} = k \frac{\partial^2 \mathbf{r}_{\alpha,l,t}}{\partial l^2} + \mathbf{g}(\alpha, l, t) \tag{4a}$$

dx.doi.org/10.1021/ma4005988 | Macromolecules 2013, 46, 4633−4650

$$F_R = \frac{k}{2}\sum_{\alpha=1}^{f}\sum_{l=0}^{N_a}(\mathbf{r}_{\alpha,l+1,t}-\mathbf{r}_{\alpha,l,t})^2 = \frac{k}{2}\sum_{\alpha=1}^{f}\int_0^{N_a}\left(\frac{\partial \mathbf{r}_{\alpha,l,t}}{\partial l}\right)^2 dl \tag{4b}$$

where $\mathbf{r} = \mathbf{r}_{\alpha,l,t}$ is the position vector of the lth segment in the arm α at time t. The Rouse segments in each arm are labeled $l = 0, 1, ..., N_a$ starting from the branch point where $l = 0$ and ending at the arm tip where $l = N_a$ (Figure 6, left).

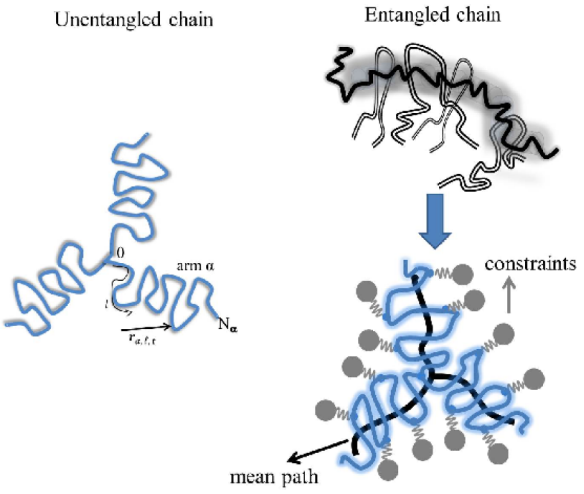

Figure 6. Left: Schematic illustration of an unentangled star. The position vector $\mathbf{r} = \mathbf{r}_{\alpha,l,t}$ of the lth segment in arm α at time t is shown. Right: The entanglements are modeled by localizing springs (constraints). The thick black line shows the mean path.

The drag is uniformly distributed all over the chain with each segment carrying an effective drag of ζ_0. The factor $k = 3k_BTb^{-2}$ is the entropic spring constant, where b is the segmental length. The term $\mathbf{g}(\alpha, l, t)$ is the Brownian force on the lth segment of the arm α with averages $\langle g(\alpha, l, t)\rangle = 0$ and $\langle g_\mu(\alpha, l, t)g_\nu(\beta, l', t')\rangle = 2\zeta_0 k_B T\delta(l - l')\delta(t - t')\delta_{\alpha\beta}\delta_{\mu\nu}$. Indices μ and ν denote Cartesian coordinates while α and β are used to label different arms. The boundary conditions of eq 4a are determined by the specific polymer architecture (linear, star, Cayley, comb, etc.).

In Appendix A, we present the appropriate boundary conditions for a symmetric star with f arms, and calculate the MSD of two segments placed at the same or different arms. We have made the approximation that the fast Rouse modes (small wavelengths) dominate the dynamics. Therefore, the expressions are strictly valid for $t \ll \tau_{R_a}$ where τ_{R_a} is the Rouse relaxation time of an arm given by $\tau_{R_a} = \tau_{mon}N_a^2$ with $\tau_{mon} = \zeta_0 b^2(3\pi^2 k_B T)^{-1}$. The obtained results are presented in Table 1. In these expressions, $\Phi(x)$ is the error function given by $\Phi(x) = 2/\sqrt{\pi}\int_0^x e^{-u^2}\,du$ and $\tilde{t}_{R_a} = |t - t'|\tau_{R_a}^{-1}$ is the time normalized by τ_{R_a}. The terms $\langle(\mathbf{r}_{\alpha,l,t} - \mathbf{r}_{\alpha,l',t'})^2\rangle$ and $\langle(\mathbf{r}_{\alpha,l,t} - \mathbf{r}_{\beta,l',t'})^2\rangle$ refer, respectively, to the MSD of segments in the same and in different arms. The expression for the segmental self-motion ($\alpha = \beta, l = l'$) is given in the third row of Table 1. This expression reduces to $\langle(\mathbf{r}_{\alpha,0,t} - \mathbf{r}_{\alpha,0,t'})^2\rangle = (2/f)(2N_a b^2/\pi^{1.5})\sqrt{\tilde{t}_{R_a}}$ (fourth row of Table 1) for the branch point, which is lower by a factor of $2/f$ compared to the segmental motion in a linear chain of polymerization degree N_a.[1,38] The expressions of Table 1 are consistent in the limit case of linear chains. Indeed if we set $f = 2$, they provide the well-known Rouse behavior for the segmental motion of unentangled linear chains. It is worth mentioning that the reduced $\langle(\mathbf{r}_{\alpha,l,t} - \mathbf{r}_{\alpha,l',t'})^2\rangle$ equation for linear chains is a closed expression, in contrast to the corresponding equation in ref 1 (eq 4.III.9 on page 134). Moreover, at equilibrium ($t = t'$) the Gaussian chain limit is recovered independently of f. Indeed the terms $\langle(\mathbf{r}_{\alpha,l,t} - \mathbf{r}_{\alpha,l',t'})^2\rangle$ and $\langle(\mathbf{r}_{\alpha,l,t} - \mathbf{r}_{\beta,l',t'})^2\rangle$ reduce, for $t = t'$, to the Gaussian chain result, $b^2|l - l'|$ and $b^2(l + l')$ respectively.

4.2. Entangled Dynamics. In a polymer melt, the entanglements imposed by the surrounding chains on a test chain localize it in space. This effect is not incorporated in eqs 4, which refer to a free chain. Therefore, for describing effects due to entanglements, an alternative model is required. Following on from earlier works[23,24,33−35] and that of Read et al.,[22] in order to model the entanglement effect, we localize each segment (α, l) of a Rouse chain by a harmonic potential centered at a fixed point $\mathbf{R}_{\alpha,l}$(Figure 6 right). The strength of the potential is parametrized by h_s. One may consider the potential as a virtual anchoring chain with N_s segments, where

Table 1. MSD of Unentangled Stars

MSD	expression
$\langle(\mathbf{r}_{\alpha,l,t} - \mathbf{r}_{\alpha,l',t'})^2\rangle$	$\frac{2N_a b^2}{\pi^{1.5}}\sqrt{\tilde{t}_{R_a}}\exp\left(\frac{-\pi^2}{4\tilde{t}_{R_a}}\frac{\lvert l-l'\rvert^2}{N_a^2}\right) - \frac{2(f-2)N_a b^2}{f\pi^{1.5}}\sqrt{\tilde{t}_{R_a}}\exp\left(\frac{-\pi^2(l+l')^2}{4N_a^2\tilde{t}_{R_a}}\right) - \frac{(f-2)b^2(l+l')}{f}\left[\Phi\left(\frac{\pi(l+l')}{2N_a\sqrt{\tilde{t}_{R_a}}}\right) - 1\right] + b^2\lvert l-l'\rvert\Phi\left(\frac{\pi\lvert l-l'\rvert}{2N_a\sqrt{\tilde{t}_{R_a}}}\right)$
$\langle(\mathbf{r}_{\alpha,l,t} - \mathbf{r}_{\beta,l',t'})^2\rangle$	$\frac{b^2(l+l')}{f}\left[(f-2) + 2\Phi\left(\frac{\pi(l+l')}{2N_a\sqrt{\tilde{t}_{R_a}}}\right)\right] + \frac{4N_a b^2}{f\pi^{1.5}}\sqrt{\tilde{t}_{R_a}}\exp\left(\frac{-\pi^2(l+l')^2}{4N_a^2\tilde{t}_{R_a}}\right)$
$\langle(\mathbf{r}_{\alpha,l,t} - \mathbf{r}_{\alpha,l,t'})^2\rangle$	$2b^2 l\left(\frac{f-2}{f}\right)\left[1 - \Phi\left(\frac{\pi l}{\sqrt{\tilde{t}_{R_a}}N_a}\right)\right] + \frac{2N_a b^2}{\pi^{1.5}}\sqrt{\tilde{t}_{R_a}}\left[1 - \left(\frac{f-2}{f}\right)\exp\left(\frac{-\pi^2 l^2}{\tilde{t}_{R_a}N_a^2}\right)\right]$
$\langle(\mathbf{r}_{\alpha,0,t} - r_{\alpha,0,t'})^2\rangle$	$\frac{2}{f}\frac{2N_a b^2}{\pi^{1.5}}\sqrt{\tilde{t}_{R_a}}$

dx.doi.org/10.1021/ma4005988 | Macromolecules 2013, 46, 4633−4650

Table 2. MSD for Entangled Stars

MSD	expression
$\langle(\mathbf{r}_{\alpha,s,t} - \mathbf{r}_{\alpha,s',t'})^2\rangle$	$a^2\lvert s-s'\rvert + a^2\sqrt{k_b}\left[\exp\left(\frac{-\lvert s-s'\rvert}{\sqrt{k_b}}\right) - \frac{(f-2)}{f}\exp\left(\frac{-(s+s')}{\sqrt{k_b}}\right)\right] - \frac{a^2\sqrt{k_b}}{2}\left[2\cosh\left(\frac{\lvert s-s'\rvert}{\sqrt{k_b}}\right) - \Omega_-^A(s,s',\tilde{t}_e) - \Omega_+^A(s,s',\tilde{t}_e)\right] + \frac{a^2\sqrt{k_b}}{2}\frac{(f-2)}{f}\left[2\cosh\left[\frac{(s+s')}{\sqrt{k_b}}\right] - \Omega_-^B(s,s',\tilde{t}_e) - \Omega_+^B(s,s',\tilde{t}_e)\right]$
$\langle(\mathbf{r}_{\alpha,s,t} - r_{\beta,s',t'})^2\rangle$	$a^2(s+s') + \frac{2a^2\sqrt{k_b}}{f}\exp\left(\frac{-(s+s')}{\sqrt{k_b}}\right) - \frac{a^2\sqrt{k_b}}{f}\left[2\cosh\left[\frac{(s+s')}{\sqrt{k_b}}\right] - \Omega_-^B(s,s',\tilde{t}_e) - \Omega_+^B(s,s',\tilde{t}_e)\right]$
$\langle(\mathbf{r}_{\alpha,s,t} - \mathbf{r}_{\alpha,s,t'})^2\rangle$	$a^2\sqrt{k_b}\,\Phi\left(\frac{\sqrt{\tilde{t}_e}}{\pi\sqrt{k_b}}\right) - \frac{a^2\sqrt{k_b}}{2}\frac{(f-2)}{f}\exp\left(\frac{-2s}{\sqrt{k_b}}\right)\left[1+\Phi\left(\frac{\sqrt{\tilde{t}_e}}{\pi\sqrt{k_b}} - \frac{\pi s}{\sqrt{\tilde{t}_e}}\right)\right] + \frac{a^2\sqrt{k_b}}{2}\frac{(f-2)}{f}\exp\left(\frac{2s}{\sqrt{k_b}}\right)\left[1-\Phi\left(\frac{\sqrt{\tilde{t}_e}}{\pi\sqrt{k_b}} + \frac{\pi s}{\sqrt{\tilde{t}_e}}\right)\right]$
$\langle(\mathbf{r}_{\alpha,0,t} - \mathbf{r}_{\alpha,0,t'})^2\rangle$	$\frac{2a^2\sqrt{k_b}}{f}\Phi\left(\frac{\sqrt{\tilde{t}_e}}{\pi\sqrt{k_b}}\right)$

where

$$\Phi(x) = \frac{2}{\sqrt{\pi}}\int_0^x e^{-u^2}\,du$$

$$\Omega_-^A(s,s',\tilde{t}_e) = \exp\left(\frac{-\lvert s-s'\rvert}{\sqrt{k_b}}\right)\Phi\left(\frac{\sqrt{\tilde{t}_e}}{\pi\sqrt{k_b}} - \frac{\pi\lvert s-s'\rvert}{2\sqrt{\tilde{t}_e}}\right);\quad \Omega_+^A(s,s',\tilde{t}_e) = \exp\left(\frac{\lvert s-s'\rvert}{\sqrt{k_b}}\right)\Phi\left(\frac{\sqrt{\tilde{t}_e}}{\pi\sqrt{k_b}} + \frac{\pi\lvert s-s'\rvert}{2\sqrt{\tilde{t}_e}}\right)$$

$$\Omega_-^B(s,s',\tilde{t}_e) = \exp\left(\frac{-(s+s')}{\sqrt{k_b}}\right)\Phi\left(\frac{\sqrt{\tilde{t}_e}}{\pi\sqrt{k_b}} - \frac{\pi(s+s')}{2\sqrt{\tilde{t}_e}}\right);\quad \Omega_+^B(s,s',\tilde{t}_e) = \exp\left(\frac{(s+s')}{\sqrt{k_b}}\right)\Phi\left(\frac{\sqrt{\tilde{t}_e}}{\pi\sqrt{k_b}} + \frac{\pi(s+s')}{2\sqrt{\tilde{t}_e}}\right)$$

$N_s = h_s^{-1}$. The Langevin equation and the free energy in this model read, respectively:

$$\zeta_0\frac{\partial\mathbf{r}_{\alpha,l,t}}{\partial t} = k\frac{\partial^2\mathbf{r}_{\alpha,l,t}}{\partial l^2} + kh_s(\mathbf{R}_{\alpha,l} - \mathbf{r}_{\alpha,l,t}) + \mathbf{g}(a,l,t) \tag{5a}$$

$$F = \frac{k}{2}\sum_{\alpha=1}^{f}\sum_{l=0}^{N_a}[(\mathbf{r}_{\alpha,l+1,t} - \mathbf{r}_{\alpha,l,t})^2 + h_s(\mathbf{R}_{\alpha,l} - \mathbf{r}_{\alpha,l,t})^2] \tag{5b}$$

where the additional terms (compared to eqs 4) involving h_s arise from the localizing potential. Each segment fluctuates about a position averaged over the entanglement relaxation time τ_e (since the $\mathbf{R}_{\alpha,l}$'s are fixed). Therefore, the position vector of each segment can be expressed as

$$\mathbf{r}_{\alpha,l,t} = \hat{\mathbf{r}}_{\alpha,l} + \mathbf{D}_{\alpha,l,t} \tag{6}$$

where $\hat{\mathbf{r}}_{\alpha,l}$ is the time-independent average position of the *l*th Rouse segment in the arm α and $\mathbf{D}_{\alpha,l,t}$ denotes the fluctuations about the average position. When all average positions are connected the mean path is obtained. As shown in ref.,[22] the mean path is obtained from eq 5b by requiring that $\partial F/\partial\mathbf{r} = 0$ at $\mathbf{r} = \hat{\mathbf{r}}_{\alpha,l}$, which yields

$$\begin{aligned}\mathbf{R}_{\alpha,l} &= \hat{\mathbf{r}}_{\alpha,l} - \frac{1}{h_s}(\hat{\mathbf{r}}_{\alpha,l+1} + \hat{\mathbf{r}}_{\alpha,l-1} - 2\hat{\mathbf{r}}_{\alpha,l})\\ &= \hat{\mathbf{r}}_{\alpha,l} - \frac{1}{h_s}\frac{\partial^2\hat{\mathbf{r}}_{\alpha,l}}{\partial l^2}\end{aligned} \tag{7}$$

When eq 7 is substituted into eq 5b, the free energy can be rewritten, in the continuous chain limit, as a sum of two independent contributions:

$$F = \underbrace{\frac{k}{2}\sum_{\alpha=1}^{f}\int_0^{N_a}\left[\left(\frac{\partial\hat{\mathbf{r}}_{\alpha,l}}{\partial l}\right)^2 + \frac{1}{h_s}\left(\frac{\partial^2\hat{\mathbf{r}}_{\alpha,l}}{\partial l^2}\right)^2\right]dl}_{\text{mean path}} + \underbrace{\frac{k}{2}\sum_{\alpha=1}^{f}\int_0^{N_a}\left[\left(\frac{\partial\mathbf{D}_{\alpha,l,t}}{\partial l}\right)^2 + h_s\mathbf{D}_{\alpha,l,t}^2\right]dl}_{\text{fluctuations}} \tag{8}$$

One depends only on the mean path (first term) and another depending only on the fluctuations about the mean path (second term). From the above equation it is apparent that the mean path contribution contains the usual Gaussian chain stretching energy term, $(k/2)(\partial\hat{\mathbf{r}}_{\alpha,l}/\partial l)^2$, and a second term

dx.doi.org/10.1021/ma4005988 | Macromolecules 2013, 46, 4633−4650

$(k/2)h_s^{-1}(\partial^2\hat{\mathbf{r}}_{\alpha,l}/\partial l^2)^2$, which penalises bending of the mean path. Equation 8 itself is adequate enough for the description of the equilibrium configuration of the chain, but does not provide any information on the conformational changes of the chain as a function of time.

To obtain the expressions for the MSD of the entangled stars we need to examine the time evolution of the fluctuation term $\mathbf{D}_{a,l,t}$. Substitution of eq 7 in eq 5a gives the appropriate Langevin equation

$$\zeta_0\frac{\partial \mathbf{D}_{a,l,t}}{\partial t} = k\frac{\partial^2 \mathbf{D}_{a,l,t}}{\partial l^2} - kh_s\mathbf{D}_{a,l,t} + \mathbf{g}(a, l, t) \quad (9)$$

$D_{\alpha,l,t}$ can be expanded as a series of eigenmodes (eq 28 of Appendix B). Here, the procedure of obtaining the MSD is briefly described. For details regarding the derivations the reader is referred to Appendix B. We note that in the remainder of this section, equations are presented in terms of tube coordinates by making the transformations $s = l/N_e$, $a^2 = N_e b^2$ (with a the tube diameter) and $\tilde{t}_e = |t - t'|/\tau_e = (N_a/N_e)^2\tilde{t}_{R_a}$. First one works out the $\langle \mathbf{D}_{\alpha,s,t}\cdot\mathbf{D}_{\alpha,s',t'}\rangle$ and $\langle \mathbf{D}_{\alpha,s,t}\cdot\mathbf{D}_{\beta,s',t'}\rangle$ terms (eqs 30 and 31 of Appendix B) by using eqs 28 and 29. Since the chains in our theory are assumed to be Gaussian we know that at equilibrium $\langle(\mathbf{r}_{\alpha,s,0} - \mathbf{r}_{\alpha,s',0})^2\rangle = a^2|s - s'|$ and $\langle(\mathbf{r}_{\alpha,s,0} - \mathbf{r}_{\beta,s',0})^2\rangle = a^2(s + s')$. Therefore, the contribution of the mean path to the MSD can be calculated by using $\langle(\hat{\mathbf{r}}_{\alpha,s} - \hat{\mathbf{r}}_{\alpha,s'})^2\rangle = a^2|s - s'| - \langle(\mathbf{D}_{\alpha,s,0} - \mathbf{D}_{\alpha,s',0})^2\rangle$ and $\langle(\hat{\mathbf{r}}_{\alpha,s} - \hat{\mathbf{r}}_{\beta,s'})^2\rangle = a^2(s + s') - \langle(\mathbf{D}_{\alpha,s,0} - \mathbf{D}_{\beta,s',0})^2\rangle$. For linear chains, these results agree with the mean path derived by Read et al.[22] Having evaluated the mean path contribution (eqs 33 of Appendix B) the final expressions are obtained using $\langle(\mathbf{r}_{\alpha,s,t} - \mathbf{r}_{\alpha,s',t'})^2\rangle = \langle(\hat{\mathbf{r}}_{\alpha,s} - \hat{\mathbf{r}}_{\alpha,s'})^2\rangle + \langle(\mathbf{D}_{\alpha,s,t} - \mathbf{D}_{\alpha,s',t'})^2\rangle$ and $\langle(\mathbf{r}_{\alpha,s,t} - \mathbf{r}_{\beta,s',t'})^2\rangle = \langle(\hat{\mathbf{r}}_{\alpha,s} - \hat{\mathbf{r}}_{\beta,s'})^2\rangle + \langle(\mathbf{D}_{\alpha,s,t} - \mathbf{D}_{\beta,s',t'})^2\rangle$. The results are presented in Table 2. The factor k_b appearing in the expressions is equal to N_s/N_e^2. The appropriate selection for k_b, according to Read et al.,[22] is $k_b = 1/4$.

The top panel of Figure 7 shows (dashed curves) our prediction for $\langle(\mathbf{r}_{\alpha,s,t} - \mathbf{r}_{\alpha,s,t'})^2\rangle/a^2$ as a function of $\tilde{t}_e$, for three different segments along the arm. The blue, green and red dashed curves correspond to $s = 0.05$ (near the branch point), $s = 0.25$ and $s = 1$ (one entanglement segment from the branch point), respectively. In the same panel, we plot (gray line) the MSD of the branch point of an unentangled star (fourth expression of Table 1), and the MSD of a segment of an unentangled linear chain (black line). The vertical shift between these two curves is $2/f$. In order to obtain the gray and black lines we have converted the corresponding expressions for the MSD (Table 1) in tube coordinates by using $\tilde{t}_{R_a} = \tilde{t}_e(N_e/N_a)^2$, $a^2 = N_e b^2$, and $s = lN_e^{-1}$ In the bottom panel of Figure 7, we plot the same MSD, normalized by $a^2\sqrt{\tilde{t}_e}$, as in the top panel. We have also included the MSD of specific segments of unentangled stars, according to $\langle(\mathbf{r}_{\alpha,l,t} - \mathbf{r}_{\alpha,l,t'})^2\rangle$ of Table 1 converted to tube coordinates. In analogy with the data sets for entangled stars, the blue, green, and red solid curves for the unentangled case correspond to $s = 0.05$, $s = 0.25$, and $s = 1$, respectively.

The bottom panel of Figure 7 shows that the segment closer to the branch point (blue dashed curve) follows at very early time scales, up to $\tilde{t}_e \approx 0.01$, the segmental dynamics of an unentangled linear chain (black line). Then a crossover to the branch point dynamics of the unentangled case occurs, for time

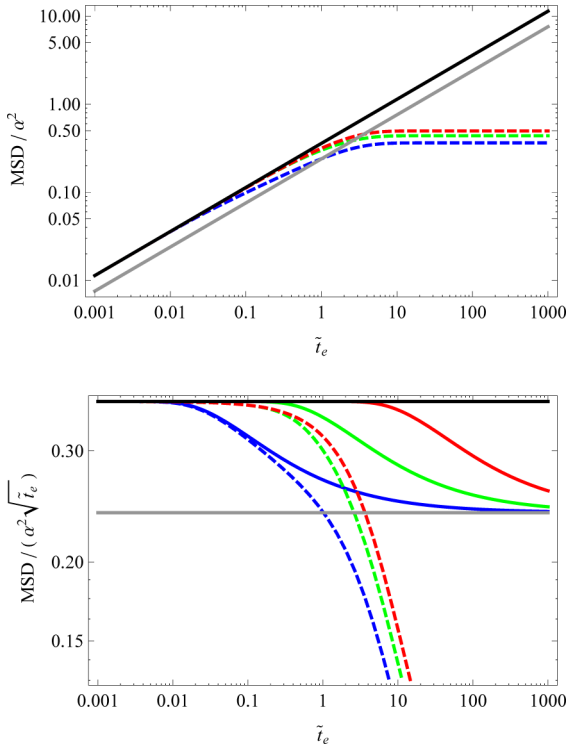

Figure 7. Top: Segmental MSD in the entangled regime ($\langle(\mathbf{r}_{\alpha,s,t} - \mathbf{r}_{\alpha,s,t'})^2\rangle$ of Table 2), normalized by a^2, for three different segments along an arm: $s = 0.05$ (blue curve), $s = 0.25$ (green), and $s = 1$ (red). The gray line corresponds to branch point motion in the unentangled regime while the black one to simple Rouse motion of an unentangled linear chain. Bottom: The same quantities as in the top panel, together with predictions for segmental motion in the unentangled regime ($\langle(\mathbf{r}_{\alpha,l,t} - \mathbf{r}_{\alpha,l,t'})^2\rangle$ of Table 1), represented as solid curves (color codes correspond to same values of s). In this case the MSD has been normalized by $a^2\sqrt{\tilde{t}_e}$. The expressions that refer to the unentangled case have been converted in tube coordinates using $\tilde{t}_{R_a} = \tilde{t}_e(N_e/N_a)^2$, $a^2 = N_e b^2$, and $s = l(N_e)^{-1}$.

scales $0.02 \lesssim \tilde{t}_e \lesssim 0.1$ (the dashed and solid blue lines coincide in this interval). At later time scales the segment starts to experience the localizing effects and a final crossover to a plateau in the MSD occurs. This plateau arises at time scales $\tilde{t}_e \gtrsim 1$ after the entanglement time, and shows up, as an horizontal line or a line of $-1/2$ slope, in the top and bottom panels of Figure 7, respectively. The other two segments that are located further from the branch point ($s = 0.25$ and $s = 1$) are localized before they feel the presence of the branch point. Subsequently, their MSD exhibits a crossover from the unentangled linear chain behavior to the plateau regime without following the branch point dynamics of the unentangled star.

At this point it must be reminded that we have assumed that motion is dominated by fast Rouse modes. Therefore, the expressions presented in Tables 1 and 2 are valid for time scales much smaller than the Rouse time of the arm, τ_{R_a}, and for segments close to the central branch point. Thus, in the next Section we will limit the comparison between the theoretical MSD and the simulation results to the case of the branch point, since it exhibits only a weak relaxation within the MD window (see Figures 2−5).

dx.doi.org/10.1021/ma4005988 | Macromolecules 2013, 46, 4633−4650

5. QUANTITATIVE EVALUATION OF MOLECULAR DYNAMICS DATA

5.1. Simulations with Fixed Chain Ends. As discussed in section 3 (Figures 2−5), in the MD simulations of entangled stars and Cayley trees several relaxation modes are active at different time scales. At early times $t < \tau_e$ the dynamics of the chain is dominated by Rouse motion. The Rouse regime is followed by local reptative motion ("Rouse in tube" dynamics) and by arm retraction depending on the position of the segment along the arm. Additionally, arm retraction contributes continuously to constraint release.[2] Since our theoretical expression for the segmental self-motion ($\langle(\mathbf{r}_{\alpha,s,t} - \mathbf{r}_{\alpha,s,t'})^2\rangle$ of Table 2) accounts only for internal Rouse modes its validity should be tested initially against MD simulations where all other relaxation mechanisms are to a high degree inactive. Accordingly, in the regime where such mechanisms are not effective we do not expect significant differences between the motion of the branch point in the simulated stars and that of the central branch point in the Cayley trees. In the remainder of the paper the data presented for the branch point motion in the Cayley tree must be understood as that of the central branch point.

With these ideas in mind, we have performed additional MD simulations of symmetric stars and Cayley trees in which the ends of the long and short arms are fixed in space. This suppresses arm retraction, as well as constraint release driven by arm retraction, and therefore it provides information that can be directly compared with the theoretical results of section 4.2. The corresponding MSD with their error bars, obtained from MD with fixed ends, for segments close to the branch point are shown in Figure 8 with open symbols. Specifically, open red circles and open blue circles refer to the MSD of the branch point in the star and Cayley tree, respectively. In the same figure their average MSD (up to time scales of $t \sim 10^6$ for which data for both branch points exist) is also shown with small close triangles. For improving statistics, the MSD is averaged over 10 monomers, namely the branch point and the three nearest monomers in each arm. For the remainder of the paper we shall refer to this group of 10 monomers as "the branch point" of the simulation. As expected, the results confirm that on the time scales relevant for our combined study there are no differences, within statistics, between the MSD of the branch point in the star and Cayley tree.

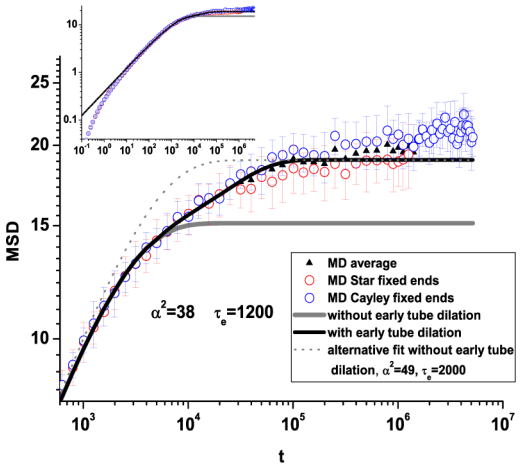

Figure 8. MD results for the MSD of the branch point of the symmetric star (open red circles) and of the central branch point of the Cayley tree (open blue circles) with their respective error bars. The close small triangles refer to the their average MSD up to $t \sim 10^6$. The full gray line corresponds to the theoretical MSD without including the early tube dilation process. The dashed gray line represents an attempt to describe the whole spectrum of the data with different set of parameters. The black line shows the theoretical prediction when early tube dilation is taken into account.

Figure 8 also includes our theoretical prediction as a full gray line. In a similar manner to the average performed in the MSD of the simulations, we have averaged over the MSD for the continuous chain between $s = 0$ and $s = 3N_e^{-1}$ for each arm. The same procedure is performed in the comparison with the case of free ends (see Figure 15 and explanation below). The theoretical MSD has been constructed by using the parameters $a^2 = 38$ and $\tau_e = 1200$. By adjusting the parameters a^2 and τ_e we can obtain agreement between the predicted MSD and simulation data in the Rouse regime or/and in the apparent plateau region, but so-obtained MSD curves fail in the description of the crossover between these two regimes at times $2000 < t < 10^5$. One example of such theoretical curve with a set of parameters $a^2 = 49$, $\tau_e = 2000$ is shown in Figure 8 with dashed gray line. Thus, we have forced the values of $a^2 = 38$ and $\tau_e = 1200$ in order to match the theoretical and the simulation MSD in the Rouse and crossover regime (compare symbols and full gray line in the inset of Figure 8 in the interval $10 \lesssim t \lesssim 10^5$). Obviously, since the model predicts Rouse dynamics at $t \to 0$, it does not account for the early ballistic motion observed in MD (see time scales $t < 10$ in the inset of Figure 8). The theoretical entanglement time $\tau_e = 1200$ is somewhat smaller than the value $\tau_e = 1800$ estimated from previous simulation MSD.[30] Nevertheless, taking into account, that local stiffness effects in the simulated chains are not implemented in the theoretical model and that there are some uncertainties in the method of τ_e estimation from the simulation, these two values of entanglement time are in a relatively good agreement.

The most noticeable feature in Figure 8 is that at times significantly beyond τ_e (i.e., times greater than 10^4), the MD data continue to rise while the theoretical MSD forms a clear plateau. As shown in section 4.2, the plateau in the theory is fully expected since no other relaxation mechanism, except internal Rouse motion, is included. In contrast, the MD data clearly indicate that, even if the arm ends are fixed, branch points remain free and it seems they can experience some relaxation of the entanglement constraints. This relaxation occurs after the branch point has explored its initial entanglement cage at the time scale τ_e.

A possible interpretation of this observation is that there is some process occurring after τ_e, giving rise to an apparent slow relaxation of the branchpoint localization. We refer to this process as a "tube dilation", as it shares some features with the processes softening the tube. However, we should bear in mind, that this process is not a dilution in a sense of widening of the tube due to "standard" constraint release from arm retraction and removal of entanglements of surrounding chains, because this relaxation mechanism is absent in this simulation. Indeed the mean path cannot relax since the arm ends are fixed and progressive dilution of the entanglement network mediated by the retraction of the arms is not possible. We can only speculate as to the mechanisms involved in this early "tube dilation" process. It could be due to tension equilibration along the constraining chains, which might relax some of the localizing potential and would occur at the Rouse time of the arms. In an

dx.doi.org/10.1021/ma4005988 | Macromolecules 2013, 46, 4633−4650

earlier work Zhou and Larson[26] investigated, by MD of a similar bead−spring model, melts of linear chains with fixed chain ends. They also reported tube dilation and attributed it to a new type of constraint release (see Figure 7 in ref 26), called "end looping" constraint release (ELCR), which occurred through Rouse motion. ELCR in melts of linear chains has also been studied at the level of primitive paths.[39] However, for strongly entangled chains this process is only effective near the chain ends,[26] and we do not expect it to be relevant for relaxation of the branch point in the systems investigated here.

An alternative possibility is that the branch point makes short excursions along the tubes of each arm ("diving modes"[40]), which in entropic terms are not so unfavorable as end looping. A precise characterization of the microscopic mechanisms involved in the early tube dilation process is beyond the scope of this work. Still, it is worth mentioning that visual inspection of branch point trajectories, in the MD simulations with fixed ends, gives some indications of the diving modes. Concretely, the branch point diving can be seen in roughly half of the branch point trajectories of Cayley tree and symmetric stars. Figure 9 shows an example for a selected star. Orange dots represent the trajectory of the branch point (plotted at intervals of $t \sim 0.1\tau_e$). The three curves formed by the black, blue, and green lines are the "mean paths" of the three arms. These have been obtained by averaging the monomer positions over the whole trajectory of the simulation with fixed arms, and provide an estimation of the tube contour. The shape of the trajectory in the figure is not spherical and reveals a deep exploration of one of the tubes (green arm) by the branch point. Such a deep withdrawal of the branch point in only one particular direction occurs rarely; in most cases, the trajectory has an elliptical or triangular shape, indicating much milder branch point excursions in two or three arm tubes.

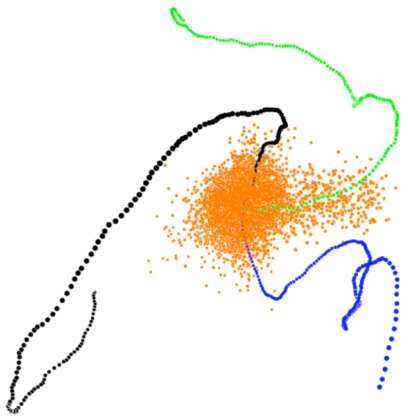

Figure 9. For a selected star in the simulations with fixed ends, trajectory of the branch point (orange dots) and mean paths of the three arms (black, blue and green). Perspective depth is used. A deep fluctuation of the branch point along the green arm is clearly observed.

Irrespective of its origin, we wish to quantify the magnitude of this apparent "tube dilation" process. This is so that when we (later) consider simulations in which the arm ends are not fixed, and constraint release is active, we can consider the *additional*, and much stronger, rescaling of the tube diameter due to constraint release, assuming that this acts as an independent process. We assume that the tube enlargement depends weakly on time so there is a separation of time scale between fast Rouse motion within the tube and a slower "tube enlargement" process. Therefore, we may still use the expression for $\langle(\mathbf{r}_{\alpha,s,t} - \mathbf{r}_{\alpha,s,t'})^2\rangle$ in Table 2 after rescaling appropriately the model parameters as

$$a^2(\Delta t) = \frac{a^2}{g(\Delta t)}, \quad \tau_e(\Delta t) = \frac{\tau_e}{g^2(\Delta t)}, \quad s(\Delta t) = s_0 g(\Delta t) \tag{10}$$

where $\Delta t = |t - t'|$. Under this renormalization the early Rouse-in-tube behavior remains unchanged. The term $g(\Delta t)$ is a slowly varying tube dilation function which is obtained by minimizing the error between the theory and the averaged branch point MD data (i.e., the small close triangles of Figure 8) using trial values in the range [0,1]. The so-obtained function $g(\Delta t)$ can be fitted to

$$g(\Delta t) = \begin{cases} g_0 + g_1, & \text{if } \Delta t \le t_0 \\ g_0 + g_1 \exp(-(\Delta t - t_0)/\tau_g), & \text{if } \Delta t > t_0 \end{cases} \tag{11}$$

with $g_0 \approx 0.75$, $g_1 \approx 0.25$, $\tau_g \approx 22600.0$, and $t_0 = 5010.0$ for both stars and Cayley trees (since the respective MSD from simulations are identical within statistics). The black line in Figure 8 represents the theoretical MSD of the branch point after incorporating the effect of tube dilation as described above. It is worth mentioning that $g(\Delta t)$ at the longest MD time approaches a value of 0.75, which can be interpreted as an increase of the original tube diameter a of the order of 15%. The effective relaxation time τ_g for the tube dilation is about five times smaller than the Rouse relaxation time of an arm.

Having analyzed the mean square displacement for the branch point in the MD with fixed arm ends, we can move on to assess the effects of constraint release in the case of the free ends. We present our findings in the following subsection.

5.2. Simulations with Free Chain Ends. Now we turn our attention to simulations with free ends (i.e., the "standard" constraint release is now active). As aforementioned, it is well established that relaxation in symmetric star-like architectures does not occur by reptation, but via activated contour length fluctuations (CLF), also referred to as arm retraction.[2] When these fluctuations are deeper than an entanglement spacing the chain has to maneuver around the entanglements in order to fluctuate. This process is associated with an entropic penalty. As the CLF from the arm tip toward the branch point become deeper, the conformation that the chain has to adopt becomes entropically more unfavorable. This leads to a very broad distribution of relaxation times, as demonstrated in Figures 2−5. In particular, the separation of relaxation time scales along a star arm is exponential.[2] During arm retraction constraint release is also occurring. When chains escape from their original tubes (by arm retraction), they induce constraint release events on other chains. Thus, the molecular strands of the arms that are still unrelaxed (entangled) after a waiting time t, are able to explore a wider tube than the original one. Because of the broad spectrum of relaxation times, this tube dilation process due to CR is typically modeled as an effective dilution of the entanglement network (see section 4.3.2 of ref 2). This approach is referred to as the "dynamic dilution hypothesis".[2] Our present simulations represent an opportunity to test this hypothesis.

For both studied systems the time τ_a taken for a complete retraction of the long arm ($Z = 8$) is not reached within the MD window. Thus, at the upper limit (2×10^7) of the

dx.doi.org/10.1021/ma4005988 | Macromolecules 2013, 46, 4633−4650

simulation time window there is an arm fraction of ≈0.3 and ≈0.4 in the star and the Cayley tree, respectively, that is still unrelaxed (see below). We take this fact into consideration and assume that branch point dynamics is still governed by chain motion within a localizing potential at the end of the MD. If we make use of the dynamic dilution hypothesis, and assume that constraint release provides an additional rescaling of the tube diameter over and above the early tube dilation process discussed in subsection 5.1, we expect that the model parameters can be renormalized in this case as

$$a^2(\Delta t) = \frac{a^2}{g(\Delta t)\psi^{\alpha_d}(\Delta t)},$$
$$\tau_e(\Delta t) = \frac{\tau_e}{g(\Delta t)^2\psi^{2\alpha_d}(\Delta t)},$$
$$s(\Delta t) = s_0 g(\Delta t)\psi^{\alpha_d}(\Delta t), \quad (12)$$

where $\psi(\Delta t)$ is the fraction of material that is still entangled (unrelaxed) after a waiting time Δt. The exponent α_d is the so-called dilution exponent, often assumed to be 1 or 4/3. In our calculations we have investigated both values of α_d (see Figure 15). The factor $g(\Delta t)$ is the function obtained in the previous section (eq 11) describing the early tube dilation process. The dilution function $\psi(\Delta t)$ corresponds to the tube survival probability.[2] We can estimate it directly from the simulations as follows. Following the original work of Doi and Edwards,[1] we formulate the tube survival probability in terms of the tangent correlation function and specify it for the case of a three-arm symmetric star:

$$\psi_l(t) = \langle \mathbf{u}_{\alpha,l,0}\cdot(\mathbf{R}^e_{\alpha,t} + B'\mathbf{R}^e_{\beta,t} + C'\mathbf{R}^e_{\gamma,t})\rangle \quad (13)$$

In this equation $\mathbf{u}_{\alpha,l,0} = \partial\mathbf{r}_{\alpha,l,0}/\partial l$ represents the tangent vector at the lth segment in the arm α at time 0. $\mathbf{R}^e_{\alpha,t} = \mathbf{r}_{\alpha,N_\alpha,t} - \mathbf{r}_{\alpha,0,t}$ is the end-to-end vector of the arm α at time t. The three indices $\alpha,\beta,\gamma \in \{1,2,3\}$ are *different* and denote the three arms of the star. The numerical coefficients B' and C' provide the weight of the correlations between the arm α and the other two arms β and γ.

Equations similar to eq 13 have been proposed,[41] but using the mean path rather than the chain coordinates. The difference between these two approaches is that the mean path includes an average over short-time internal modes of the chain. We now demonstrate that, with suitably chosen coefficients B' and C', eq 13 does not decay due to local Rouse motion of the chain within the tube, and so it is not necessary to use the mean path. We demonstrate this by evaluating eq 13 for *unentangled* three-arm symmetric stars. To do so, we express the tangent vector $\mathbf{u}_{\alpha,l,0}$ and the end to end vectors $\mathbf{R}^e_{\alpha,t}$, $\mathbf{R}^e_{\beta,t}$, $\mathbf{R}^e_{\gamma,t}$ in terms of the Rouse modes using eq 18 of Appendix A. Regarding the coefficients B', C', we consider first the case $B' = C' = -1/2$ ("half-correlation"). The final expression reads

$$\psi_l(t) = \frac{4b^2}{\pi}\sum_p \frac{1}{2p-1}\times\left[\cos\left(\frac{(2p-1)\pi s_l}{2}\right)\right.$$
$$\left.\sin\left(\frac{(2p-1)\pi}{2}\right)\exp\left(\frac{-\tilde{t}_{R_a}(2p-1)^2}{4}\right)\right] \quad (14)$$

where $s_l = l/N_a$ and $\tilde{t}_{R_a} = t/\tau_{R_a}$. In Figure 10, eq 14 is plotted (solid lines) as a function of the normalized time $\tilde{t}_{R_a}$ for

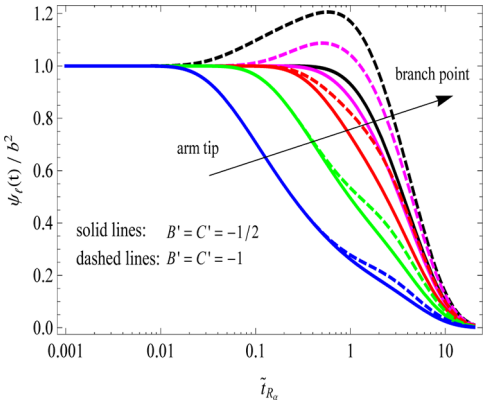

Figure 10. Tangent correlation function (eq 13) for unentangled stars. The solid lines refer to 'half-correlation' (i.e., $B' = C' = -1/2$) while the dashed lines to "full-correlation" (i.e., $B' = C' = -1$). Different colors correspond to different Rouse segments along the arm, $s_l = 0.15$ (black), 0.3 (magenta), 0.5 (red), 0.7 (green), and 0.85 (blue).

different values of s_l. In the usual continuous approximation, the sum in the former equation extends from $p = 1$ to $p = p_{max} \to \infty$. For the numerical calculation, we used $p_{max} = 1000$. Results for larger p_{max} were indistinguishable from those of Figure 10. The figure demonstrates that, for inner sections of the chain, the "half-correlation" function starts to decay at around τ_{R_a} indicating that it is insensitive to higher order Rouse modes. For sections of chain close to chain ends, the initial decay is seen at a time scale set by the Rouse time of the $(1 - s_l)$ section of the chain (i.e., by $\tau_R(s_l) = \tau_{mon}N_a^2(1 - s_l)^2$). Short length scale Rouse modes never lead to decay of the function. Therefore, the use of chain coordinates instead of the mean path has no significant effect on our calculations. The same applies when tube dilation is present. This is because tube dilation will not affect the decay of $\psi_l(t)$, as it simply introduces a few more fast Rouse modes to average over.

We also considered the option $B' = C' = -1$ ("full-correlation"). As seen from the dashed lines in Figure 10, by including the full correlations between the star arms, the obtained function $\psi_l(t)$ exceeds the maximum expected value, i.e., $\psi_l(t) > 1.0$ and gives undesirable peaks for segments close to the branch point ($s_l = 0.15, 0.3$). To avoid this effect, we take into consideration only the half correlation ($B' = C' = -1/2$) when we calculate eq 13, for entangled stars, using the simulation data (see below). The final choice of the prefactors B' and C' for particular segments of the star and Cayley tree is illustrated in Figure 11. Note that each arm of the Cayley tree is divided into three different parts (outer segments, inner segments, short arm), so there are more terms on the right side of eq 13 (and more than two prefactors B',C' are needed, see Figure 11 b.)). For the Cayley tree and the star arm indices α,β,γ denote in this case different parts of the molecule (e.g., in Figure 11 b.), α refers to the inner arm, β and γ would refer to the two other inner arms, with prefactors of $-1/2$ each, and a fourth symbol is required for the outer arm, with prefactor -1).

We move on to the entangled systems. We calculated the tangent correlation function (eq 13) by using the simulation data. Thus, the tangent vector in eq 13 was approximated by the end-to-end vector of an arm segment of length equal to ten monomeric units. This segment size was chosen as a compromise to both achieving good statistics and averaging

dx.doi.org/10.1021/ma4005988 | Macromolecules 2013, 46, 4633−4650

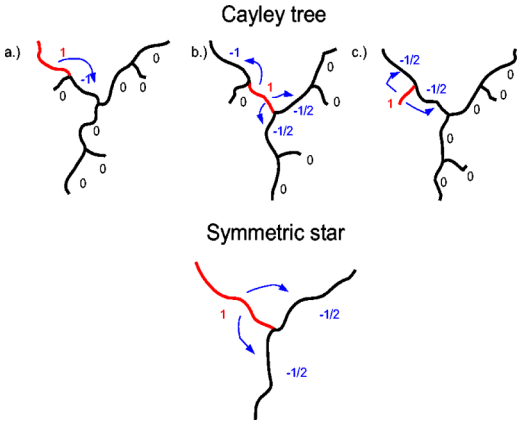

Figure 11. Schematic representation of the correlations used for the correlator $\psi_l(t)$. Numbers labeling particular segments are the prefactors B' and C' used in eq 13 and red color highlights the segment l on the arm/part α. Parts a and b show the correlations of the outer and inner segments of the long arm of the Cayley tree. Part c illustrates the correlations of the short arm segments of the Cayley tree.

fast monomer fluctuations (not captured within the coarse-grained tube model). In Figure 12 we show the time evolution

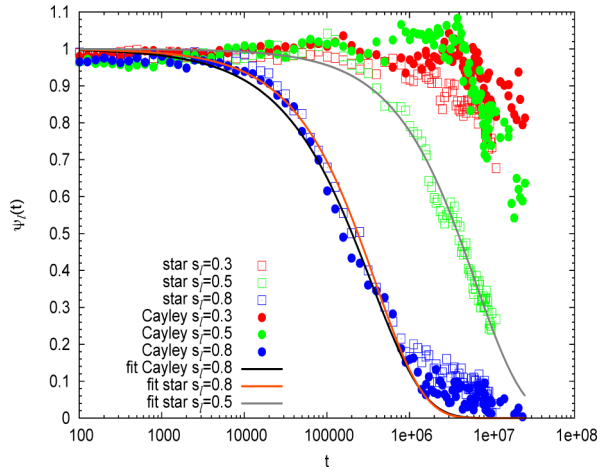

Figure 12. Tangent correlation functions for the segments of symmetric star (squares) and Cayley tree (circles) with the fitting KWW functions.

of the so-obtained correlation functions for different segments s_l of the symmetric stars and Cayley trees. It is clear that not all the functions fully relax within the MD time window. In particular, inner segments remain, on average, confined in their tubes—e.g., for $s_l = 0.3$ the tube survival probability barely drops to the value $\psi_l(t) = 0.8$ at the end of the simulation. The tangent correlators $\psi_l(t)$ were fitted to stretched exponential (Kohlraus–William–Watts, KWW) functions:

$$\psi_l(t) = \exp(-(t/\tau_l)^{\beta}) \tag{15}$$

where β is the stretching exponent and τ_l is the relaxation time of the lth-segment. From the fitting procedure we get a set of points$[s_l; \tau_l]$, that provides us the information about the consecutive relaxation of the segments along the arms. We can use this information to construct functions $\Xi_{\alpha,\beta,\gamma}(t)$ that represent the fraction of unrelaxed material of the star arms or Cayley tree's parts α,β,γ. The function is normalized so that $\Xi_{\alpha,\beta,\gamma}(0) = 1$ (all the material is unrelaxed at $t = 0$), and it decays with time in an exponential-like fashion, until all the material is relaxed, $\Xi_{\alpha,\beta,\gamma}(\tau_{N_a}) = 0$.

The procedure for obtaining the function $\Xi_\alpha(t)$ is illustrated in Figure 13 for the case of the stars (obviously the function is

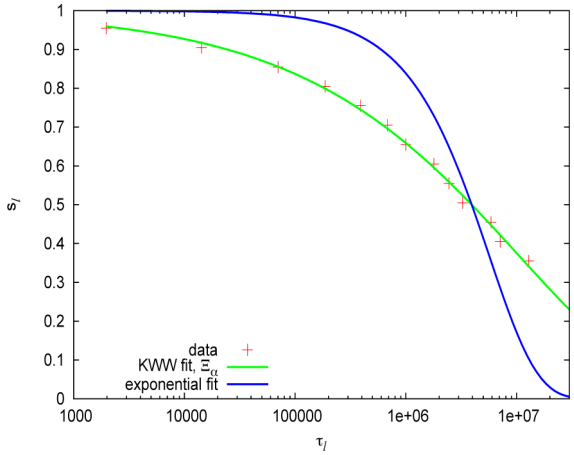

Figure 13. Symbols: for the stars, KWW times of the tangent correlators $\psi_l(t)$ versus the respective coordinates s_l. Curves: fits to exponential (blue) and KWW behavior (green).

identical for the three arms α,β,γ). There we show the coordinates s_l versus the respective KWW times τ_l, obtained from fitting the tangent correlators $\psi_l(t)$ as described above. This gives us a "discrete" representation of the time elapsed for relaxing the fraction of the arm tube extending from $s = 1$ (arm tip) to $s = s_l$. Likewise, the fraction from $s = s_l$ to $s = 0$ (branch point) will be the fraction of unrelaxed tube at time $t = \tau_l$. By fitting the discrete set of points in Figure 13 to some model function, we will obtain the continuous functions $\Xi_{\alpha,\beta,\gamma}(t)$ describing the tube survival probability of each arm $\{\alpha,\beta,\gamma\}$. Two model functions have been used in the fit, namely an exponential (blue curve in Figure 13) and a KWW function (green line). The data show strong deviations from pure exponential behavior and are much better described by a KWW function. As aforementioned, in the star $\Xi_\alpha(t)$ is identical for the three arms. In the case of the Cayley tree, we have three sets of points $[s_l; \tau_l]$ for each arm, since this consists of three parts: outer segments, inner segments, and short side branch. Thus, we performed fits for the three sets of data to obtain their (nonidentical) functions $\Xi_\alpha(t)$.

Then, having the full description of the time evolution of the relaxation of the star arms and Cayley tree's parts, there is just a small step from the functions $\Xi_\alpha(t),\Xi_\beta(t),\Xi_\gamma(t)$ to the total tube survival probability $\psi(t)$ of the star and Cayley tree. The total tube survival probability can be calculated as:

$$\psi(t) = \frac{Z_\alpha\Xi_\alpha + Z_\beta\Xi_\beta + Z_\gamma\Xi_\gamma}{Z_\alpha + Z_\beta + Z_\gamma} \tag{16}$$

where Z_α is the number of entanglements per star arm or Cayley tree's part α. The functions $\psi(t)$ for the symmetric star and Cayley tree are shown in Figure 14. Note that these *model* functions, constructed by following the fitting procedure described above, extend beyond the MD time window ($t \gtrsim$

dx.doi.org/10.1021/ma4005988 | Macromolecules 2013, 46, 4633–4650

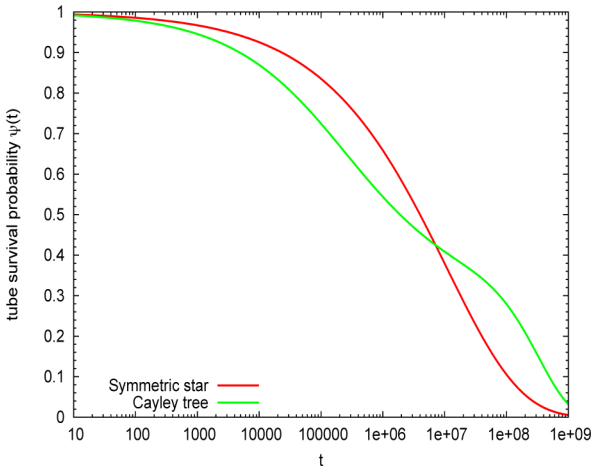

Figure 14. Tube survival probability of the symmetric star and the Cayley tree, obtained from the simulations.

10^7), and fully decay at $t \sim 10^9$, but we note this is simply a possible extrapolation of the data. Nothing that follows depends on this. At the end of the MD, the decay is $\psi(t) \approx 0.3$ and 0.4 for the star and Cayley tree, respectively. Interestingly, the fraction of unrelaxed material is larger in the star than in the Cayley tree up to time scales of $t \approx 7 \times 10^6$. Then the two curves $\psi(t)$ cross each other, and at longer times tube relaxation is much faster in the stars. The observed behavior seems consistent with an initially stronger tube dilution in the Cayley trees, being facilitated by the presence of the weakly entangled side branches. Indeed these relax in a time scale of about $t \approx 10^6$, i.e, roughly in the time window for which the stars show a higher $\psi(t)$. In hierarchical models, after their full relaxation the side branches act as friction points, and the Cayley tree reduces to a star containing "fat beads" originating from the relaxed side branches. This additional friction slows down the retraction of the long arms, and relaxation of the Cayley tree at long times becomes slower than in the stars. This picture seems consistent with the trends observed in Figure 14.

Finally, we use the tube survival probability estimated from the simulations to obtain the theoretical MSD of the branch point. The latter, as predicted by $\langle(\mathbf{r}_{\alpha,s,t} - \mathbf{r}_{\alpha,s,t'})^2\rangle$ of Table 2, and using the rescaling parameters of eq 12, is represented in Figure 15 with solid cyan lines and solid magenta lines for $\alpha_d = 1$ and $\alpha_d = 4/3$, respectively. In the same figure the simulation data with free ends are depicted with open black circles together with their respective error bars. Note that in the majority of cases the width of the error bar is of a similar size to the width of the black open circle. The top panel refers to the symmetric star while the bottom panel to the Cayley tree. For comparison we include the data of the simulation with fixed ends (small red and small blue circles), previously presented in Figure 8. Since constraint release is now active, the MSD of the branch point is larger than its counterpart in the MD with fixed ends (compare the open black circles with the small close circles at time scales bigger than $t \sim 10^5$). Moreover, in the time window $10^3 \lesssim t \lesssim 5 \times 10^6$ the branch point in the star is more localized than in the Cayley tree, since at these time scales $\psi(t)$ of the star is bigger than $\psi(t)$ of the Cayley tree (see Figure 14).

From Figure 15, it is clear that our theoretical prediction agrees very well with the MD data for the case $\alpha_d = 1$. Our results demonstrate that one can use the tube survival

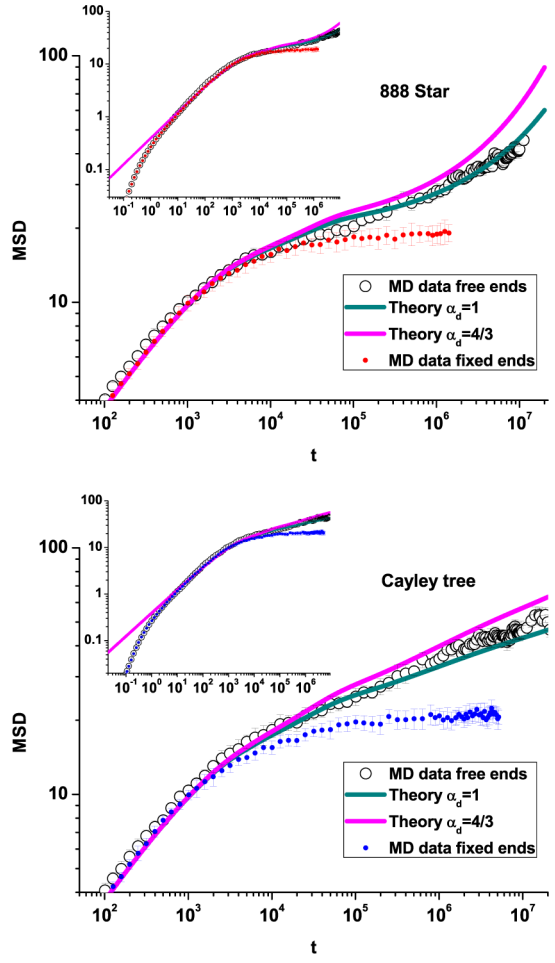

Figure 15. MSD of the branch point of the symmetric stars (top) and Cayley trees (bottom) with free ends. MD data are shown as open black circles. Their error is also shown with black bars. The solid cyan (magenta) curve corresponds to the theoretical MSD using $\alpha_d = 1$ ($\alpha_d = 4/3$) and accounts for CR events and the early tube dilation process. For comparison we also include the MD data for fixed arm ends (small close circles with their error bars).

probability, parametrized by $\psi(t)$, to predict the effective dilution of the tube diameter, measured from the mean square displacement of the branch point. This observation is a strong confirmation of the "dynamic dilution" hypothesis. It remains possible that a higher value of the dilution exponent, such as 4/3, could be used, but this would require some form of partial tube dilation, as (for example) suggested by Watanabe et al.[18]

6. CONCLUSIONS

We have presented large-scale computer simulations of entangled polymers with symmetric star-like and Cayley tree-like architectures. Unlike the observation for reptation behavior of linear chains, the simulated systems exhibit a strong dispersion, over several decades, of the relaxation times after the local reptative ("Rouse in tube") regime. In particular relaxation is dramatically slowed down when approaching the branch point from the outer segments. This is consistent with the expected retraction mechanism for relaxation of strongly entangled arms in branched architectures.

We have derived analytical expressions describing local motion of branched chains subject to entanglement constraints. The model provides a generalization of the Rouse regime for

dx.doi.org/10.1021/ma4005988 | Macromolecules 2013, 46, 4633−4650

symmetric star-like architectures and introduces entanglements by localizing springs. Predictions of the model for localization of the branch point have been compared with simulations with fixed arm ends, which suppress retraction and constraint release. Strikingly, the simulations reveal that, in contrast with the model, the mean square displacement continues to grow weakly with increasing time, despite the absence of constraint-release effects. Possible mechanisms for this include tube dilution due to tension equilibration along surrounding chains, and branch point diving along the star-arm tubes (we have found some evidence of the latter). We have quantified the strength of this early tube dilation process, as well as the fraction of unrelaxed material in the simulation with free ends. This allows us to renormalize the tube diameter and entanglement time as time-dependent quantities. With this renormalization, our model provides an excellent description of the mean square displacement of the branch point. The fact that we were able to use the tube survival probability, measured from correlation functions within the simulation, to predict the effective dilution of the tube diameter, measured from the mean square displacement of the branch-point, is a strong confirmation of the physics underlying the 'dynamic dilution' hypothesis.

Our analytical model can be used for making predictions for other observables. Thus, the first two expressions of Table 2 can be used for the calculation of the dynamic structure factor of a star, for example when treating experimental neutron spin echo data.[42] Work in this direction is in progress.

APPENDIX

A. MSD Unentangled Regime

The appropriate boundary conditions for a symmetric star with f arms are

$$\mathbf{r}_{\alpha=1,l=0,t} = \mathbf{r}_{\alpha=2,l=0,t} = ... = \mathbf{r}_{\alpha=f,l=0,t} \tag{17a}$$

$$\frac{\partial \mathbf{r}}{\partial l}|_{\alpha=1,l=0} + \frac{\partial \mathbf{r}}{\partial l}|_{\alpha=2,l=0} + ... + \frac{\partial \mathbf{r}}{\partial l}|_{\alpha=f,l=0} = 0 \tag{17b}$$

$$\frac{\partial \mathbf{r}}{\partial l}|_{\alpha=1,l=N_a} = \frac{\partial \mathbf{r}}{\partial l}|_{\alpha=2,l=N_a} = ... = \frac{\partial \mathbf{r}}{\partial l}|_{\alpha=f,l=N_a} = 0 \tag{17c}$$

Equation 17a satisfies the chain connectivity requirement at the branch point while eq 17b represents the force balance at the branch point. Equation 17c indicates that there is no external force acting at the free ends of the arms. Under the previous boundary conditions, $\mathbf{r}_{\alpha,l,t}$ can be expressed as a series of eigenmodes, in particular one cosine eigenmode and $f' = f - 1$ sine eigenmodes,[43,44] indexed with the mode numbers p and q

$$\mathbf{r}_{\alpha,l,t} = \sum_p \mathbf{X}_p^c(t)\Psi_p^c(l) + \sum_q (\mathbf{X}_q^{s_1}(t)\Psi_q^{s_1}(\alpha, l) + ... + \mathbf{X}_q^{s_{f'}}(t)\Psi_q^{s_{f'}}(\alpha, l)) \tag{18}$$

with

$$\Psi_p^c(l) = \cos\left(\frac{p\pi l}{N_a}\right) \tag{19a}$$

$$\Psi_q^{s_i}(\alpha, l) = s_{i\alpha} \sin\left(\frac{(2q-1)\pi l}{2N_a}\right) \tag{19b}$$

The numerical coefficients $s_{i\alpha}$ satisfy the following constraints

$$\sum_{\alpha=1}^{f} s_{i\alpha} = 0 \tag{20a}$$

$$\sum_{\alpha=1}^{f} {s_{i\alpha}}^2 = f \tag{20b}$$

$$\sum_{\alpha=1}^{f} s_{i\alpha}s_{j\alpha} = 0 \tag{20c}$$

where indices i,j denote the ith and jth eigenmode, respectively. Equation 20a is a consequence of the force balance at the branch point (eq 17b). Equations 20b and 20c arise from normalization and orthogonality, respectively.

The first step towards the calculation of the MSD is to substitute eq 18 into eq 4a and operate from the left the resulting expression with the following integral operators

$$\sum_{\alpha=1}^{f}\int_0^{N_a}\sum_{p'}\Psi_{p'}^c(l)\,\mathrm{d}l, \quad \sum_{\alpha=1}^{f}\int_0^{N_a}\sum_{q'}\Psi_{q'}^{s_1}(\alpha, l)\,\mathrm{d}l, \quad ..., \quad \sum_{\alpha=1}^{f}\int_0^{N_a}\sum_{q'}\Psi_{q'}^{s_{f'}}(\alpha, l)\,\mathrm{d}l$$

After making use of eqs 20 (only 'diagonal' terms, which contain products of the form $\Psi_{p'}^c\Psi_p^c$, $\Psi_{q'}^{s_i}\Psi_q^{s_i}$, are nonzero because of eqs 20a and 20c), the following set of f decoupled equations for the time evolution of the eigenmodes amplitudes $\mathbf{X}_p^c(t),\mathbf{X}_p^{s_1}(t),...,\mathbf{X}_p^{s_f'}(t)$ is obtained

$$\begin{aligned}
\zeta_p\frac{\partial \mathbf{X}_p^c(t)}{\partial t} &= -k_p^c\mathbf{X}_p^c(t) + \mathbf{g}_p^c(t)\\
\zeta_q\frac{\partial \mathbf{X}_q^{s_1}(t)}{\partial t} &= -k_q^{s_1}\mathbf{X}_q^{s_1}(t) + \mathbf{g}_q^{s_1}(t)\\
&\vdots\\
\zeta_q\frac{\partial \mathbf{X}_q^{s_{f'}}(t)}{\partial t} &= -k_q^{s_{f'}}\mathbf{X}_q^{s_{f'}}(t) + \mathbf{g}_q^{s_{f'}}(t)
\end{aligned} \tag{21}$$

All equations that refer to sine eigenmodes are identical so in practice only two of the above equations need to be solved. In particular, the one that refers to $\mathbf{X}_p^c(t)$ and one of the remaining $f-1$ that refer to $\mathbf{X}_q^{s_1}(t) = ... = \mathbf{X}_q^{s_{f'}}(t) = \mathbf{X}_q^{s_i}(t)$. In the system of eqs 21, $\zeta_p = \zeta_q = (f\zeta_0N_a/2)$, $k_p^c = ((fp^2\pi^2 3k_BT)/(2N_ab^2))$, $k_q^{s_i} = ((f(2q-1)^2\pi^2 3k_BT)/(8N_ab^2))$ and

$$\mathbf{g}_p^c(t) = \sum_{\alpha=1}^{f}\int_0^{N_a}\mathbf{g}(\alpha, l, t)\Psi_p^c\,\mathrm{d}l \tag{22a}$$

$$\mathbf{g}_q^{s_i}(t) = \sum_{\alpha=1}^{f}\int_0^{N_a}\mathbf{g}(\alpha, l, t)\Psi_q^{s_i}\,\mathrm{d}l \tag{22b}$$

The solutions for $\mathbf{X}_p^c(t)$ and $\mathbf{X}_q^{s_i}(t)$ are obtained using the integrating factor method and are

$$\mathbf{X}_p^c(t) = \frac{\exp\left(-\frac{t}{\tau_p^c}\right)}{\zeta_p}\int_{-\infty}^{t}\mathbf{g}_p^c\exp\left(\frac{t'}{\tau_p^c}\right)\mathrm{d}t' \tag{23a}$$

dx.doi.org/10.1021/ma4005988 | Macromolecules 2013, 46, 4633−4650

$$\mathbf{X}_q^{s_i}(t) = \frac{\exp\left(-\frac{t}{\tau_q^{s_i}}\right)}{\zeta_q}\int_{-\infty}^{t}\mathbf{g}_q^{s_i}\exp\left(\frac{t'}{\tau_q^{s_i}}\right)\mathrm{d}t' \tag{23b}$$

where $\tau_p^c = \zeta_p(k_p^c)^{-1}$ and $\tau_q^{s_i} = \zeta_q(k_q^{s_i})^{-1}$.

The next step is to compute the $\langle X_{p_\mu}^c(t)X_{p'_\nu}^c(t')\rangle$ and $\langle X_{q_\mu}^{s_i}(t)X_{q'_\nu}^{s_i}(t')\rangle$ averages. To do this, one first needs to work out the averages that involve the noise terms, namely $\langle g_{p_\mu}^c g_{p'_\nu}^c\rangle$ and $\langle g_{q_\mu}^{s_i} g_{q'_\nu}^{s_i}\rangle$ using eqs 22a and 22b and $\langle g_\mu(\alpha,l,t)g_\nu(\beta,l',t')\rangle = 2\zeta_0 k_B T\delta(l-l')\delta(t-t')\delta_{\alpha\beta}\delta_{\mu\nu}$, and then use eqs 23a and 23b. The "nondiagonal" averages of the form $\langle X_{p_\mu}^c(t)X_{q'_\nu}^{s_i}(t')\rangle$, $\langle X_{q_\mu}^{s_i}(t)X_{q'_\nu}^{s_j}(t')\rangle$ vanish since they contain orthogonal terms like $\Psi_p^c\Psi_{q'}^{s_i}$ and $\Psi_q^c\Psi_{q'}^{s_j}$. The final expressions are

$$\langle \mathbf{X}_p^c(t)\cdot\mathbf{X}_{p'}^c(t')\rangle = \frac{2N_a b^2\delta_{pp'}}{f\pi^2 p^2}\exp(-\tilde{t}_{R_a}p^2) \tag{24a}$$

$$\langle \mathbf{X}_q^{s_i}(t)\cdot\mathbf{X}_{q'}^{s_i}(t')\rangle = \frac{8N_a b^2\delta_{qq'}}{f\pi^2(2q-1)^2}\exp\left(\frac{-\tilde{t}_{R_a}(2q-1)^2}{4}\right) \tag{24b}$$

where $\tilde{t}_{R_a} = |t-t'|\tau_{R_a}^{-1}$. The time scale τ_{R_a} is the Rouse relaxation time of an arm of N_a monomers and is given by $\tau_{R_a} = \zeta_0 b^2 N_a^2(3\pi^2 k_B T)^{-1}$. At equilibrium the previous expressions reduce to $\langle \mathbf{X}_p^c(0)\cdot\mathbf{X}_{p'}^c(0)\rangle = ((2N_a b^2\delta_{pp'})/(f\pi^2 p^2))$ and $\langle \mathbf{X}_q^{s_i}(0)\cdot\mathbf{X}_{q'}^{s_i}(0)\rangle = ((8N_a b^2\delta_{qq'})/(f\pi^2(2q-1)^2))$. We mention that $\langle \mathbf{X}_p^c(0)\cdot\mathbf{X}_{p'}^c(0)\rangle$ and $\langle \mathbf{X}_q^{s_i}(0)\cdot\mathbf{X}_{q'}^{s_i}(0)\rangle$ can be calculated by making use of the equipartition theorem, after substitution of eq 18 into the free energy of the system (eq 4b).

Having obtained the correlation functions of the mode amplitudes it is a straightforward procedure to obtain the expressions for the MSD. In order to obtain the final expressions for $\langle(\mathbf{r}_{\alpha,l,t}-\mathbf{r}_{\alpha,l',t'})^2\rangle$ and $\langle(\mathbf{r}_{\alpha,l,t}-\mathbf{r}_{\beta,l',t'})^2\rangle$ we need to calculate $\langle \mathbf{r}_{\alpha,l,t}\cdot\mathbf{r}_{\alpha,l',t'}\rangle$ and $\langle \mathbf{r}_{\alpha,l,t}\cdot\mathbf{r}_{\beta,l',t'}\rangle$. The results read

$$\begin{aligned}\langle \mathbf{r}_{\alpha,l,t}\cdot\mathbf{r}_{\alpha,l',t'}\rangle &= \langle[\sum_p \mathbf{X}_p^c(t)\Psi_p^c(l) \\ &+ \sum_q(\mathbf{X}_q^{s_1}(t)\Psi_q^{s_1}(\alpha,l) + \ldots + \mathbf{X}_q^{s_{f'}}(t)\Psi_q^{s_{f'}}(\alpha,l))] \\ &\times[\sum_{p'}\mathbf{X}_{p'}^c(t')\Psi_{p'}^c(l') + \sum_{q'}(\mathbf{X}_q^{s_1}(t')\Psi_q^{s_1}(\alpha,l') + \ldots \\ &+ \mathbf{X}_q^{s_{f'}}(t')\Psi_q^{s_{f'}}(\alpha,l'))]\rangle = \frac{N_a b^2}{\pi^2}\left[\int_0^\infty \frac{\cos\left(\frac{p\pi|l-l'|}{N_a}\right)}{p^2}\right. \\ &\exp(-\tilde{t}_{R_a}p^2)\,\mathrm{d}p - \left(\frac{f-2}{f}\right)\int_0^\infty\frac{\cos\left(\frac{p\pi(l+l')}{N_a}\right)}{p^2} \\ &\left.\exp(-\tilde{t}_{R_a}p^2)\,\mathrm{d}p\right] = -\frac{N_a b^2}{\pi^{1.5}}\sqrt{\tilde{t}_{R_a}}\exp\left(-\frac{\pi^2|l-l'|^2}{4N_a^2\tilde{t}_{R_a}}\right) \\ &-\frac{b^2|l-l'|}{2}\Phi\left(\frac{\pi|l-l'|}{2N_a\sqrt{\tilde{t}_{R_a}}}\right) + \frac{N_a b^2}{\pi^{1.5}}\left(\frac{f-2}{f}\right)\sqrt{\tilde{t}_{R_a}} \\ &\exp\left(-\frac{\pi^2(l+l')^2}{4N_a^2\tilde{t}_{R_a}}\right) + \frac{b^2(l+l')}{2}\left(\frac{f-2}{f}\right)\Phi\left(\frac{\pi(l+l')}{2N_a\sqrt{\tilde{t}_{R_a}}}\right)\end{aligned} \tag{25}$$

and

$$\begin{aligned}\langle \mathbf{r}_{\alpha,l,t}\cdot\mathbf{r}_{\beta,l',t'}\rangle &= \langle[\sum_p \mathbf{X}_p^c(t)\Psi_p^c(l) \\ &+ \sum_q(\mathbf{X}_q^{s_1}(t)\Psi_q^{s_1}(\alpha,l) + \ldots + \mathbf{X}_q^{s_{f'}}(t)\Psi_q^{s_{f'}}(\alpha,l))] \\ &\times[\sum_{p'}\mathbf{X}_{p'}^c(t')\Psi_{p'}^c(l') + \sum_{q'}(\mathbf{X}_q^{s_1}(t')\Psi_q^{s_1}(\beta,l') + \ldots \\ &+ \mathbf{X}_q^{s_{f'}}(t')\Psi_q^{s_{f'}}(\beta,l'))]\rangle = \frac{2N_a b^2}{f\pi^2}\int_0^\infty\frac{\cos\left(\frac{p\pi(l+l')}{N_a}\right)}{p^2} \\ &\exp(-\tilde{t}_{R_a}p^2)\,\mathrm{d}p = -\frac{2N_a b^2}{f\pi^{1.5}}\sqrt{\tilde{t}_{R_a}}\exp\left(-\frac{\pi^2(l+l')^2}{4N_a^2\tilde{t}_{R_a}}\right) \\ &-\frac{b^2(l+l')}{f}\Phi\left(\frac{\pi(l+l')}{2N_a\sqrt{\tilde{t}_{R_a}}}\right)\end{aligned} \tag{26}$$

In the derivation of eqs 25, 26 we have used eqs 18 and 24 and $s_{1\alpha}{}^2+\ldots+s_{f'\alpha}{}^2 = f-1$, $s_{1\alpha}s_{1\beta}+\ldots+s_{f'\alpha}s_{f'\beta} = -1$. Moreover, we have approximated the sums as integrals and we have assumed $2p-1 = 2p$, $2q-1 = 2q$, which physically means that the fast Rouse modes (large p, q) dominate the dynamics. For the evaluation of the integrals we have used

dx.doi.org/10.1021/ma4005988 | Macromolecules 2013, 46, 4633−4650

$$\int_0^\infty \frac{\cos(\bar{A}x) \times \exp(-\bar{B}x^2)}{x^2}\,dx = -\sqrt{\pi\bar{B}}\,\exp\left(\frac{-\bar{A}^2}{4\bar{B}}\right) - \frac{\bar{A}\pi}{2}\Phi\left(\frac{\bar{A}}{2\sqrt{\bar{B}}}\right), \quad \bar{A},\ \bar{B} \geq 0$$

From eq 25, we arrive at

$$\langle \mathbf{r}_{\alpha,l,t}\cdot\mathbf{r}_{\alpha,l,t}\rangle = \frac{(f-2)}{f}b^2 l \tag{27a}$$

$$\langle \mathbf{r}_{\alpha,l',t'}\cdot\mathbf{r}_{\alpha,l',t'}\rangle = \frac{(f-2)}{f}b^2 l' = \langle \mathbf{r}_{\beta,l',t'}\cdot\mathbf{r}_{\beta,l',t'}\rangle \tag{27b}$$

By substituting eqs 25, 26 and 27 into

$$\langle(\mathbf{r}_{\alpha,l,t} - \mathbf{r}_{\alpha,l',t'})^2\rangle = \langle \mathbf{r}_{\alpha,l,t}\cdot\mathbf{r}_{\alpha,l,t}\rangle + \langle \mathbf{r}_{\alpha,l',t'}\cdot\mathbf{r}_{\alpha,l',t'}\rangle - 2\langle \mathbf{r}_{\alpha,l,t}\cdot\mathbf{r}_{\alpha,l',t'}\rangle$$

$$\langle(\mathbf{r}_{\alpha,l,t} - \mathbf{r}_{\beta,l',t'})^2\rangle = \langle \mathbf{r}_{\alpha,l,t}\cdot\mathbf{r}_{\alpha,l,t}\rangle + \langle \mathbf{r}_{\beta,l',t'}\cdot\mathbf{r}_{\beta,l',t'}\rangle - 2\langle \mathbf{r}_{\alpha,l,t}\cdot\mathbf{r}_{\beta,l',t'}\rangle$$

one obtains the first and second expressions of Table 1.

B. MSD Entangled Regime

The fluctuation term $\mathbf{D}_{\alpha,l,t}$ can be expanded as a series of eigenmodes, in particular cosine eigenmodes with degeneracy 1 and sine eigenmodes with degeneracy $f' = f - 1$, indexed with the mode numbers p and q, respectively,

$$\mathbf{D}_{\alpha,l,t} = \sum_p \mathbf{Y}^c_p(t)\Psi^c_p(\alpha, l) + \sum_q (\mathbf{Y}^{s_1}_q(t)\Psi^{s_1}_q(\alpha, l) + \ldots + \mathbf{Y}^{s_{f'}}_q(t)\Psi^{s_{f'}}_q(\alpha, l)) \tag{28}$$

The expansion is performed in a similar manner to eq 18 of Appendix A. The eigenmodes Ψ^c_p and $\Psi^{s_1}_q$, ..., $\Psi^{s_{f'}}_q$ are the same as in eq 18, and their explicit expressions are given by eqs 19. The eigenmode amplitudes $\mathbf{Y}^c_p$ and $\mathbf{Y}^{s_i}_q$ differ from those of the unentangled case ($\mathbf{X}^c_p$ and $\mathbf{X}^{s_i}_q$) because of the additional $-kh_s\mathbf{D}_{a,l,t}$ term (compare the structure of eqs 4a and 9). The correlation functions $\langle \mathbf{Y}^c_p(t)\cdot\mathbf{Y}^c_{p'}(t')\rangle$ and $\langle \mathbf{Y}^{s_i}_q(t)\cdot\mathbf{Y}^{s_i}_{q'}(t')\rangle$, are calculated following exactly the same procedure as for the calculation of $\langle \mathbf{X}^c_p(t)\cdot\mathbf{X}^c_{p'}(t')\rangle$ and $\langle \mathbf{X}^{s_i}_q(t)\cdot\mathbf{X}^{s_i}_{q'}(t')\rangle$ in the unentangled case (see Appendix B). The final expressions are

$$\langle \mathbf{Y}^c_p(t)\cdot\mathbf{Y}^c_{p'}(t')\rangle = \frac{2N_a b^2\delta_{pp'}}{f\pi^2\left[p^2 + \left(\sqrt{h_s}\frac{N_a}{\pi}\right)^2\right]} \times \exp\left(-\tilde{t}_{R_a}\left[p^2 + \left(\sqrt{h_s}\frac{N_a}{\pi}\right)^2\right]\right) \tag{29a}$$

$$\langle \mathbf{Y}^{s_i}_q(t)\cdot\mathbf{Y}^{s_i}_{q'}(t')\rangle = \frac{8N_a b^2\delta_{qq'}}{f\pi^2\left[(2q-1)^2 + \left(2\sqrt{h_s}\frac{N_a}{\pi}\right)^2\right]} \times \exp\left(-\frac{1}{4}\tilde{t}_{R_a}\left[(2q-1)^2 + \left(2\sqrt{h_s}\frac{N_a}{\pi}\right)^2\right]\right) \tag{29b}$$

In Appendix B we calculated the $\langle \mathbf{r}_{\alpha,l,t}\cdot\mathbf{r}_{\alpha,l',t'}\rangle$ and $\langle \mathbf{r}_{\alpha,l,t}\cdot\mathbf{r}_{\beta,l',t'}\rangle$ correlation functions. A similar calculation can be performed for $\langle \mathbf{D}_{\alpha,l,t}\cdot\mathbf{D}_{\alpha,l',t'}\rangle$ and $\langle \mathbf{D}_{\alpha,l,t}\cdot\mathbf{D}_{\beta,l',t'}\rangle$. The differences between the two cases are: one should use eqs 28 and 29 instead of eqs 18 and 24, and the final integrals are of different form. In the latter case, one should use the following expression[45]

$$\int_0^\infty \frac{\cos(\bar{A}x)}{x^2 + \bar{C}^2} \times \exp(-\bar{B}x^2)\,dx = \frac{\pi}{4\bar{C}}\exp(\bar{B}\bar{C}^2) \times \left[2\cosh(\bar{A}\bar{C}) - \exp(-\bar{C}\bar{A}) \times \Phi\left(\bar{C}\sqrt{\bar{B}} - \frac{\bar{A}}{2\sqrt{\bar{B}}}\right) - \exp(\bar{C}\bar{A})\Phi\left(\bar{C}\sqrt{\bar{B}} + \frac{\bar{A}}{2\sqrt{\bar{B}}}\right)\right]; \quad \bar{A},\ \bar{B} \geq 0,\ \bar{C} > 0$$

The results are expressed in tube coordinates using the transformation rules $\tilde{t}_{R_a} = \tilde{t}_e(N_e^2)/(N_a^2)$, $a^2 = N_e b^2 = (N_s k_b^{-1})^{1/2} b^2$ (recall that $N_s = h_s^{-1}$), $s = l/N_e$ as

$$\langle \mathbf{D}_{\alpha,s,t}\cdot\mathbf{D}_{\alpha,s',t'}\rangle = \frac{a^2\sqrt{k_b}}{4}\left[2\cosh\left(\frac{|s-s'|}{\sqrt{k_b}}\right) - \frac{(f-2)}{f}2\cosh\left(\frac{(s+s')}{\sqrt{k_b}}\right)\right] - \frac{a^2\sqrt{k_b}}{4}[\Omega^A_-(s, s', \tilde{t}_e) + \Omega^A_+(s, s', \tilde{t}_e)] + \frac{a^2\sqrt{k_b}}{4}\frac{(f-2)}{f}[\Omega^B_-(s, s', \tilde{t}_e) + \Omega^B_+(s, s', \tilde{t}_e)] \tag{30}$$

and

$$\langle \mathbf{D}_{\alpha,s,t}\cdot\mathbf{D}_{\beta,s',t'}\rangle = \frac{a^2\sqrt{k_b}}{2f}\left[2\cosh\left(\frac{(s+s')}{\sqrt{k_b}}\right) - \Omega^B_+(s, s', \tilde{t}_e) - \Omega^B_-(s, s', \tilde{t}_e)\right] \tag{31}$$

The functions $\Omega^A_-(s,s',\tilde{t}_e)$, $\Omega^A_+(s,s',\tilde{t}_e)$, $\Omega^B_-(s,s',\tilde{t}_e)$, $\Omega^B_+(s,s',\tilde{t}_e)$ are defined in Table 2. Moreover, from eq 30 we obtain

$$\langle \mathbf{D}_{\alpha,s,t}\cdot\mathbf{D}_{\alpha,s,t}\rangle = \frac{a^2\sqrt{k_b}}{2}\left[1 - \frac{(f-2)}{f}\exp\left(\frac{-2s}{\sqrt{k_b}}\right)\right] \tag{32a}$$

$$\langle \mathbf{D}_{\alpha,s',t'}\cdot\mathbf{D}_{\alpha,s',t'}\rangle = \langle \mathbf{D}_{\beta,s',t'}\cdot\mathbf{D}_{\beta,s',t'}\rangle = \frac{a^2\sqrt{k_b}}{2}\left[1 - \frac{(f-2)}{f}\exp\left(\frac{-2s'}{\sqrt{k_b}}\right)\right] \tag{32b}$$

From eqs 30, 31, and 32, $\langle(\mathbf{D}_{\alpha,s,t} - \mathbf{D}_{\alpha,s',t'})^2\rangle$ and $\langle(\mathbf{D}_{\alpha,s,t} - \mathbf{D}_{\beta,s',t'})^2\rangle$, and consequently their equilibrium expressions ($t = t' = 0$), are easily obtained. The chains in this model are considered Gaussian, thus at equilibrium $\langle(\mathbf{r}_{\alpha,s,0} - \mathbf{r}_{\alpha,s',0})^2\rangle = a^2|s - s'|$ and $\langle(\mathbf{r}_{\alpha,s,0} - \mathbf{r}_{\beta,s',0})^2\rangle = a^2(s + s')$. Subsequently, the contribution of the mean path to the MSD can be calculated using

$$\langle(\hat{\mathbf{r}}_{\alpha,s} - \hat{\mathbf{r}}_{\alpha,s'})^2\rangle = a^2|s - s'| - \langle(\mathbf{D}_{\alpha,s,0} - \mathbf{D}_{\alpha,s',0})^2\rangle$$

$$\langle(\hat{\mathbf{r}}_{\alpha,s} - \hat{\mathbf{r}}_{\beta,s'})^2\rangle = a^2(s + s') - \langle(\mathbf{D}_{\alpha,s,0} - \mathbf{D}_{\beta,s',0})^2\rangle$$

The result is

for segments on the same arm:

dx.doi.org/10.1021/ma4005988 | Macromolecules 2013, 46, 4633−4650

$$\langle(\hat{\mathbf{r}}_{\alpha,s} - \hat{\mathbf{r}}_{\alpha,s'})^2\rangle = a^2|s - s'| - a^2\sqrt{k_b}\left[1 - \exp\left(-\frac{|s - s'|}{\sqrt{k_b}}\right)\right] + \frac{a^2\sqrt{k_b}}{2}\left(\frac{f-2}{f}\right)\left[\exp\left(-\frac{s}{\sqrt{k_b}}\right) - \exp\left(-\frac{s'}{\sqrt{k_b}}\right)\right]^2 \quad (33a)$$

for segments on different arms:

$$\langle(\hat{\mathbf{r}}_{\alpha,s} - \hat{\mathbf{r}}_{\beta,s'})^2\rangle = a^2(s + s') - a^2\sqrt{k_b} + \frac{2a^2\sqrt{k_b}}{f}\exp\left(\frac{-(s+s')}{\sqrt{k_b}}\right) + \frac{a^2\sqrt{k_b}}{2}\left(\frac{f-2}{f}\right)\left[\exp\left(-\frac{2s}{\sqrt{k_b}}\right) + \exp\left(-\frac{2s'}{\sqrt{k_b}}\right)\right] \quad (33b)$$

To complete the derivation of the expressions for the MSD we use $\langle(\mathbf{r}_{\alpha,s,t} - \mathbf{r}_{\alpha,s',t'})^2\rangle = \langle(\hat{\mathbf{r}}_{\alpha,s} - \hat{\mathbf{r}}_{\alpha,s'})^2\rangle + \langle(\mathbf{D}_{\alpha,s,t} - \mathbf{D}_{\alpha,s',t'})^2\rangle$ and $\langle(\mathbf{r}_{\alpha,s,t} - \mathbf{r}_{\beta,s',t'})^2\rangle = \langle(\hat{\mathbf{r}}_{\alpha,s} - \hat{\mathbf{r}}_{\beta,s'})^2\rangle + \langle(\mathbf{D}_{\alpha,s,t} - \mathbf{D}_{\alpha,s',t'})^2\rangle$. The results are presented in Table 2.

AUTHOR INFORMATION

Corresponding Author

*E-mail: (A.J.M.) wabmosea@ehu.es.

Notes

The authors declare no competing financial interest.

ACKNOWLEDGMENTS

We specially acknowledge financial support from the project FP7-PEOPLE-2007-1-1-ITN (DYNACOP, Marie Curie Network, European Union), as well as from MAT2012-31088 (Spain) and IT-436-07 (GV, Spain). We acknowledge the programs PRACE, HPC-Europa2 and ESMI (European Union), and ICTS (Spain) for generous allocation of CPU time at GENCI (Paris, France), HLRS (Stuttgart, Germany), FZJ-JSC (Jülich, Germany), and CESGA (Santiago de Compostela, Spain).

REFERENCES

(1) Doi, M.; Edwards, S. F. *The Theory of Polymer Dynamics*, 1st ed.; Clarendon Press: Oxford, U.K., 1986.
(2) McLeish, T. C. B. Tube theory of entangled polymer dynamics. *Adv. Phys.* **2002**, *51*, 1379−1527.
(3) Graham, R. S.; Likhtman, A. E.; McLeish, T. C. B.; Milner, S. T. Microscopic theory of linear, entangled polymer chains under rapid deformation including chain stretch and convective constraint release. *J. Rheol.* **2003**, *47*, 1171−1200.
(4) Read, D. J. Convective constraint release with chain stretch: Solution of the Rouse-tube model in the limit of infinite tubes. *J. Rheol.* **2004**, *48*, 349−377.
(5) Ianniruberto, G.; Marrucci, G. A multi-mode CCR model for entangled polymers with chain stretch. *J. Non-Newtonian Fluid Mech.* **2002**, *102*, 383−395.
(6) Milner, S. T.; McLeish, T. C. B. Reptation and contour-length fluctuations in melts of linear polymers. *Phys. Rev. Lett.* **1998**, *81*, 725−728.
(7) Ball, R. C.; McLeish, T. C. B. Dynamic dilution and the viscosity of star polymer melts. *Macromolecules* **1989**, *22*, 1911−1913.
(8) Milner, S. T.; McLeish, T. C. B. Parameter-free theory for stress relaxation in star polymer melts. *Macromolecules* **1997**, *30*, 2159−2166.
(9) McLeish, T. C. B.; Allgaier, J.; Bick, D. K.; Bishko, G.; Biswas, P.; Blackwell, R. J.; Blottière, B.; Clarke, N.; Gibbs, B.; Groves, D. J.; Hakiki, A.; Heenan, R. K.; Johnson, J. M.; Kant, R.; Read, D. J.; Young, R. N. Dynamics of entangled H-polymers: Theory, rheology, and neutron-scattering. *Macromolecules* **1999**, *32*, 6734−6758.
(10) Lee, J. H.; Fetters, L. J.; Archer, L. A. Stress relaxation of branched polymers. *Macromolecules* **2005**, *38*, 10763−10771.
(11) McLeish, T. C. B.; Larson, R. G. Molecular constitutive equations for a class of branched polymers: The pom-pom polymer. *J. Rheol.* **1998**, *42*, 81−110.
(12) Daniels, D. R.; McLeish, T. C. B.; Crosby, B. J.; Young, R. N.; Fernyhough, C. M. Molecular rheology of comb polymer melts. 1. Linear viscoelastic response. *Macromolecules* **2001**, *34*, 7025−7033.
(13) Inkson, N. J.; Graham, R. S.; McLeish, T. C. B.; Groves, D. J.; Fernyhough, C. M. Viscoelasticity of monodisperse comb polymer melts. *Macromolecules* **2006**, *39*, 4217−4227.
(14) Kapnistos, M.; Kirkwood, K. M.; Ramirez, J.; Vlassopoulos, D.; Leal, L. G. Nonlinear rheology of model comb polymers. *J. Rheol.* **2009**, *53*, 1133−1153.
(15) Ahmadi, M.; Bailly, C.; Keunings, R.; Nekoomanesh, M.; Arabi, H.; Van Ruymbeke, E. Time marching algorithm for predicting the linear rheology of monodisperse comb polymer melts. *Macromolecules* **2011**, *44*, 647−659.
(16) Lentzakis, H.; Vlassopoulos, D.; Read, D. J.; Lee, H.; Chang, T.; Driva, P.; Hadjichristidis, N. Uniaxial extensional rheology of well-characterized comb polymers. *J. Rheol.* **2013**, *57*, 605−625.
(17) Blackwell, R. J.; Harlen, O. G.; McLeish, T. C. B. Theoretical linear and nonlinear rheology of symmetric treelike polymer melts. *Macromolecules* **2001**, *34*, 2579−2596.
(18) Watanabe, H.; Matsumiya, Y.; Van Ruymbeke, E.; Vlassopoulos, D.; Hadjichristidis, N. Viscoelastic and dielectric relaxation of a Cayley-tree-type polyisoprene: Test of molecular picture of dynamic tube dilation. *Macromolecules* **2008**, *41*, 6110−6124.
(19) Hutchings, L. R.; Kimani, S. M.; Hoyle, D. M.; Read, D. J.; Das, C.; McLeish, T. C. B.; Chang, T.; Lee, H.; Auhl, D. In silico molecular design, synthesis, characterization, and rheology of dendritically branched polymers: Closing the design loop. *ACS Macro Lett.* **2012**, *1*, 404−408.
(20) Read, D. J.; Auhl, D.; Das, C.; Den Doelder, J.; Kapnistos, M.; Vittorias, I.; McLeish, T. C. B. Linking models of polymerization and dynamics to predict branched polymer structure and flow. *Science* **2011**, *333*, 1871−1874.
(21) Hoyle, D. M.; Huang, Q.; Auhl, D.; Hassell, D.; Rasmussen, H. K.; Skov, A. L.; Harlen, O. G.; Hassager, O.; McLeish, T. C. B. Transient overshoot extensional rheology of long-chain branched polyethylenes: Experimental and numerical comparisons between filament stretching and cross-slot flow. *J. Rheol.* **2013**, *57*, 293−313.
(22) Read, D. J.; Jagannathan, K.; Likhtman, A. E. Entangled polymers: Constraint release, mean paths, and tube bending energy. *Macromolecules* **2008**, *41*, 6843−6853.
(23) Deam, R. T.; Edwards, S. F. The theory of rubber elasticity. *Philos. Trans. R. Soc. London, Ser. A* **1976**, *280*, 317−353.
(24) Warner, M.; Edwards, S. F. Neutron scattering from strained polymer networks. *J. Phys. A: Math. Gen.* **1978**, *11*, 1649−1655.
(25) Kremer, K.; Grest, G. S. Dynamics of entangled linear polymer melts: A molecular-dynamics simulation. *J. Chem. Phys.* **1990**, *92*, 5057−5086.
(26) Zhou, Q.; Larson, R. G. Direct Calculation of the Tube Potential Confining Entangled Polymers. *Macromolecules* **2006**, *39*, 6737−6743.
(27) Sukumaran, S. K.; Likhtman, A. E. Modeling entangled dynamics: Comparison between stochastic single-chain and multichain models. *Macromolecules* **2009**, *42*, 4300−4309.

(28) Wang, Z.; Likhtman, A. E.; Larson, R. G. Segmental Dynamics in Entangled Linear Polymer Melts. *Macromolecules* **2012**, *45*, 3557−3570.
(29) Auhl, A.; Everaers, R.; Grest, G. S.; Kremer, K.; Plimpton, S. J. Equilibration of long chain polymer melts in computer simulations. *J. Chem. Phys.* **2003**, *119*, 12718−12728.
(30) Zhou, Q.; Larson, R. G. Direct Molecular Dynamics Simulation of Branch Point Motion in Asymmetric Star Polymer Melts. *Macromolecules* **2007**, *40*, 3443−3449.
(31) Everaers, R.; Sukumaran, S. K.; Grest, G. S.; Svaneborg, C.; Sivasubramanian, A.; Kremer, K. Rheology and Microscopic Topology of Entangled Polymeric Liquids. *Science* **2004**, *303*, 823−826.
(32) Limbach, H. J.; Arnold, A.; Mann, B. A.; Holm, C. ESPResSo-an extensible simulation package for research on soft matter systems. *Comput. Phys. Commun.* **2006**, *174*, 704−727.
(33) Vilgis, T. A.; Boue, F. Brownian motion of chains and crosslinks in a permanently linked network: The dynamic form factor. *J. Polym. Sci., Part B: Polym. Phys.* **1988**, *26*, 2291−2302.
(34) Read, D. J. Calculation of scattering from stretched copolymers using the tube model: Incorporation of the effect of elastic inhomogeneities. *Macromolecules* **2004**, *37*, 5065−5092.
(35) Mergell, B.; Everaers, R. Tube models for rubber-elastic systems. *Macromolecules* **2001**, *34*, 5675−5686.
(36) Lee, J. H.; Fetters, L. J.; Archer, L. A. Branch-point motion in asymmetric star Polymers. *Macromolecules* **2005**, *38*, 4484−4494.
(37) Masubuchi, Y.; Yaoita, T.; Matsumiya, Y.; Watanabe, H. Primitive chain network simulations for asymmetric star polymers. *J. Chem. Phys.* **2011**, *134*, 194905.
(38) Rouse, P. E., Jr. A theory of the linear viscoelastic properties of dilute solutions of coiling polymers. *J. Chem. Phys.* **1953**, *21*, 1272−1280.
(39) Anogiannakis, S. D.; Tzoumanekas, C.; Theodorou, D. N. Microscopic Description of Entanglements in Polyethylene Networks and Melts: Strong, Weak, Pairwise, and Collective Attributes. *Macromolecules* **2012**, *45*, 9475−9492.
(40) Klein, J. Dynamics of entangled linear, branched, and cyclic polymers. *Macromolecules* **1986**, *19*, 105−118.
(41) Qin, J.; Milner, S. T.; Stephanou, P. S.; Mavratzas, V. G. Effects of tube persistence length on dynamics of mildly entangled polymers. *J. Rheol.* **2012**, *56*, 707−723.
(42) Zamponi, M.; Pyckhout-Hintzen, W.; Wischnewski, A.; Monkenbusch, M.; Willner, L.; Kali, G.; Richter, D. Molecular observation of branch point motion in star polymer melts. *Macromolecules* **2010**, *43*, 518−524.
(43) Zimm, B. H.; Kilb, R. W. Dynamics of branched polymer molecules in dilute solution. *J. Polym. Sci.* **1959**, *37*, 19−42.
(44) Watanabe, H.; Yoshida, H.; Kotaka, T. Model calculation for viscoelastic and dielectric relaxation functions of non-entangled star chains with arm length distribution. *Polym. J.* **1990**, *22*, 153−161.
(45) *Table of Integrals, Series, and Products*; Jeffrey, A., Zwillinger, D., Eds.; Elsevier: Amsterdam, 2007; Chapter 3.